THE FLORIDA STATE UNIVERSITY

COLLEGE OF ARTS AND SCIENCES

A THREE-DIMENSIONAL SIMULATION OF COASTAL UPWELLING OFF OREGON

By

Monty B. Peffley

A Thesis submitted to
the Department of Oceanography
in partial fulfillment of the
requirements for the degree of
Master of Science

Approved:

James J. O'Brien
Professor Directing Thesis

Steven Blumsack

Raymond C. Hale

Steven Blumsack

Raymond C. Hale

Richard T. Iverson

John W. Winchester
Chairman, Department of
Oceanography

March, 1975

ABSTRACT

The wind-driven, numerical, x-y-t two-layer β-plane model developed by Hurlburt (1974) is used to investigate the effects of an Oregon-like bottom topography and coastline configuration on the onset and decay of the ocean upwelling circulation. The digitized nearshore Oregon bathymetry is analyzed for dominant scales, and a smoothed version is used in model cases with several different initial states and wind stresses. Cases with topography are compared to cases with flat ocean bottoms. Topographic variations are found to dominate over coastline irregularities in determining the longshore distribution of upwelling. Results indicate that stronger upwelling observed near Cape Blanco is primarily due to the local bottom topography and not the cape itself. Observed variations in the meridional and zonal flow are explained in terms of the topographic β effect. In particular, during spin-up with an equatorward wind stress, regions favored by topography develop a nearshore poleward undercurrent. Upper layer poleward flow is observed during spin-down. The existence of an onshore transport jet south of Cape Blanco is predicted. Zonal mass balance is not observed. Topographic Rossby waves are excited during spin-up. Baroclinic continental shelf waves are observed in time series of the pycnocline height contours.

ACKNOWLEDGMENTS

I wish to thank Dr. James J. O'Brien for serving as my major professor and for his continuing support and direction of my research. Also, my thanks to Harley E. Hurlburt for allowing me to use his model and for his support and guidance.

Thanks are due Drs. Steve Blumsack, Richard Iverson and Raymond Staley for serving as members of my Master's committee. My appreciation is given to John D. Lee, J. Dana Thompson and John Kindle for their friendship and help. The excellent assistance of Sandra Fuller during my stay at the National Center for Atmospheric Research (NCAR) is gladly acknowledged.

I am grateful to Richard Berler and Dennis Dix for their painstaking care in the digitization of the bottom topography and to Dewey Rudd of the Department of Meteorology, Florida State University for his preparation of several of the figures. Elizabeth Smedley expertly improved the quality of the computer drawn figures. The NCAR Graphics Department helped to prepare Figure 3.

I was supported during my Master's program at Florida State by grants from the Office of Naval Research and from the

I was supported during my Master's program at Florida State by grants from the Office of Naval Research and from the

Coastal Upwelling Ecosystems Analysis Program, a program of

the International Decade of Ocean Exploration under the sponsorship of the National Science Foundation (Grant GX-33502).

Computer resources were granted to me by the National Center for Atmospheric Research which is sponsored by the National Science Foundation. Computations were done at NCAR on the CDC 6600 and 7600, and at Florida State on the CDC 6500.

My thanks to Joyce McKeller and to Chris Muise for typing many draft versions of this paper and to Janina Richards for typing the final manuscript.

With gratitude I acknowledge that the satisfaction felt in completion of this work will be shared by my wife Mara, who has shared in the sacrifice at all stages of the doing.

TABLE OF CONTENTS

LIST OF TABLES

LIST OF ILLUSTRATIONS

the region of greatest interest. (b) Smoothed bottom topography heights in m obtained by smoothing the topography of Fig. 4a as explained in the text. This figure shows the coastline

used in both figures 61

1. INTRODUCTION

Coastal upwelling has been the subject of much recent worldwide research. Interest has been stimulated by the remarkable influence this physical phenomenon has on the biological productivity of the coastal ecosystem. Coastal upwelling areas are extremely fertile; in fact, it has been estimated by Ryther (1969) that over half of the world's fish supply may depend upon food produced in upwelling regions. Local coastal climate is also affected by upwelling, due mainly to the band of anomalously cold surface water near the coast. For a general review of upwelling, the reader is referred to the excellent article by Smith (1968). A summary of the observational knowledge and present theory of coastal upwelling dynamics has been given by Mooers and Allen (1973). O'Brien (1975) has reviewed the modeling of coastal upwelling.

This work is part of an intensive program of observational and theoretical research known as the Coastal Upwelling Ecosystems Analysis Program (CUEA). Several large-scale observational field programs have been carried out by CUEA; two of these have focused on a portion of the coastal upwelling area near Newport, Oregon. The Coastal Upwelling

welling area near Newport, Oregon. The Coastal Upwelling
Experiment - I (CUE-I) was conducted during the summer of

1972 and was followed in the summer of 1973 by CUE II. These experiments, plus a continuing research effort by Oregon State University, have made the Oregon coast one of the world's most intensively studied coastal upwelling areas.

Another of the goals of CUEA has been to encourage development of better models of the coastal upwelling circulation. The present study follows work by several authors at Florida State University who have used two-layer numerical models to study upwelling. In particular, O'Brien and Hurlburt (1972) created a two-layer x-z model which used an efficient semi-implicit scheme. They postulated the existence of a longshore surface jet in the upwelling region. Hurlburt and Thompson (1973) demonstrated that the beta effect provides an ocean interior which produces the dynamically important longshore pressure gradient. Hurlburt (1974) added the longshore dimension to the two-layer model of Hurlburt and Thompson, thus allowing inclusion of longshore variability in the dependent variable field and forcing functions. Thompson (1974) has incorporated thermodynamics and vertical turbulence into the x-z numerical model, extending the time scale of its applicability. He has been able to simulate surface temperature fronts and the observed two-celled circulation of the upwelling regime.

the observed two-celled circulation of the upwelling regime.

Many investigators have recognized the need to understand the three-dimensional aspects of upwelling. In particular, it has long been suspected that longshore variations in bottom topography and coastline are an important factor in determining the details of the upwelling flow field. However, advances in this area have been few, leading Mooers and Allen (1973) to comment: "There is, at the present, a lack of almost any guidance from theoretical studies on what the effects of alongshore variations in topography may be. Progress on the answer to that question is badly needed." The numerical model developed by Hurlburt (1974) allows inclusion of longshore variation in bottom topography and coastline, but has so far been applied only to fairly simple and highly idealized topography and coastline configurations. As noted in the report of the June 24, 1974 meeting of the SCOR*Working Group 36 on Coastal Upwelling Processes: 'Theoretical modeling has still to develop further by taking into account more realistic features of bottom topography, coastline geometry, . . ."

The present study has been conceived as the first attempt, using the x-y-t, two-layer model of Hurlburt (1974), to study the effects of the actual coastline and bottom topography of a mesoscale coastal upwelling region, namely, that of the Oregon coast. We hope to examine relationships

graphy of a mesoscale coastal upwelling region, namely, that of the Oregon coast. We hope to examine relationships

---

*SCOR is the Scientific Committee on Oceanic Research.

between important longshore scales of geometry forcing and the associated response of the flow field. Also, we intend to compare results with the extensive observational knowledge of the Oregon region.

In this work, we are guided by several important theoretical studies in the three-dimensional aspects of upwelling and longshore variability. In particular, Arthur (1965) and Yoshida (1967) have discussed the effects of capes on steady-state flows, both concluding that the strongest upwelling should occur on the south side of capes. Suginohara (1974) studied the effects of longshore variability in the wind stress in a model with a straight coast and longshore-independent bottom topography. For a flat bottom case he found that after the winds were shut off the upwelled portion of the pycnocline propagated poleward at the speed of an internal Kelvin wave. Also, for a case with y-independent shelf-slope topography, Suginohara's model develops a poleward flow in the lower layer and exhibits northward-propagating continental shelf waves. Gill and Clarke (1974) also studied the effects of longshore variations in the equatorward wind stress and found Kelvin wave and continental shelf wave dynamics to be important in understanding the local upwelling intensity. The correlation between movements of the thermocline and changes in sea level at the coast has led them to suggest the possibility of a working procedure for the prediction of upwelling. Hurlburt (1974)

showed that the β effect simulated by north-south sloping topography plays a fundamental role in the dynamics associated with mesoscale longshore topography variations. Hurlburt found that longshore variations in topography produce barotropic flows which extend far beyond the topographic feature. Variations in coastline geometry were observed to excite large amplitude internal Kelvin waves. Recently, Pedlosky (1974a) has examined the relationship between local longshore currents and upwelling, and the scales of the longshore stress. Effects of a longshore-independent shelf-like topography have been investigated in a three-dimensional, continuously stratified f-plane model for the steady and time-dependent cases by Pedlosky (1974b, 1974c). Shaffer (1974) found that longshore variations in the topography of the NW African shelf determined the distribution of onshore flow and upwelling for that area. He proposed a homogeneous, f-plane model with a shelf whose edge varies in the longshore direction (but with no sloping topography) to explain the observed "funneling" of onshore transport.

In the present work, several cases are examined in order to study the onset, and the initial stage of relaxation, of coastal upwelling in a hydrodynamic model with Oregon-like topography. We find that longshore topographic variations favor two specific regions of the Oregon coast with respect to upwelling, and that in general, topographic variations

are dominant over coastline irregularities in affecting the upwelling patterns. Variations in the strength of longshore and lower layer onshore flow are explained by the topographic β effect. In particular, two areas next to the coast develop a poleward undercurrent during spin-up. With winds shut off, poleward flow is seen in certain areas in the upper layer.

Zonal mass balance is not observed for the Oregon upwelling area. Topographic Rossby waves are found to play an important part in the barotropic N-S flow. During spin-down, baroclinic continental shelf waves are observed in the model solutions.

2. THE MODEL

The model used in this study was developed by Hurlburt (1974). It is a wind driven, x-y-t, two-layer primitive equation model on the β-plane. The model is non-linear and retains the free surface.

a. Model geometry

Fig. 1 depicts a typical section of the appropriate geometry for application of the model to an eastern ocean coastal upwelling case. The origin of the right-handed Cartesian coordinate system is located at the easternmost extent of the fluid, at a specified latitude and at an arbitrary reference level below or level with the greatest depth of the fluid. Beta-plane approximations apply.

The two-layer fluid is contained in a channel of horizontal dimensions L_x and L_y. The western boundary is a straight solid wall, while the eastern boundary is variable. As discussed below, the northern and southern boundaries are open. As shown in Fig. 1, D(x,y) is the height of the bottom above an arbitrary reference level. The subscripts 1 and 2 refer to the upper and lower layers, respectively, throughout this paper. In particular, h_1 and h_2 are the instantaneous layer thicknesses. Notice, as indicated in Fig. 1, that the interface between the two layers is not allowed to intersect the bottom topography.

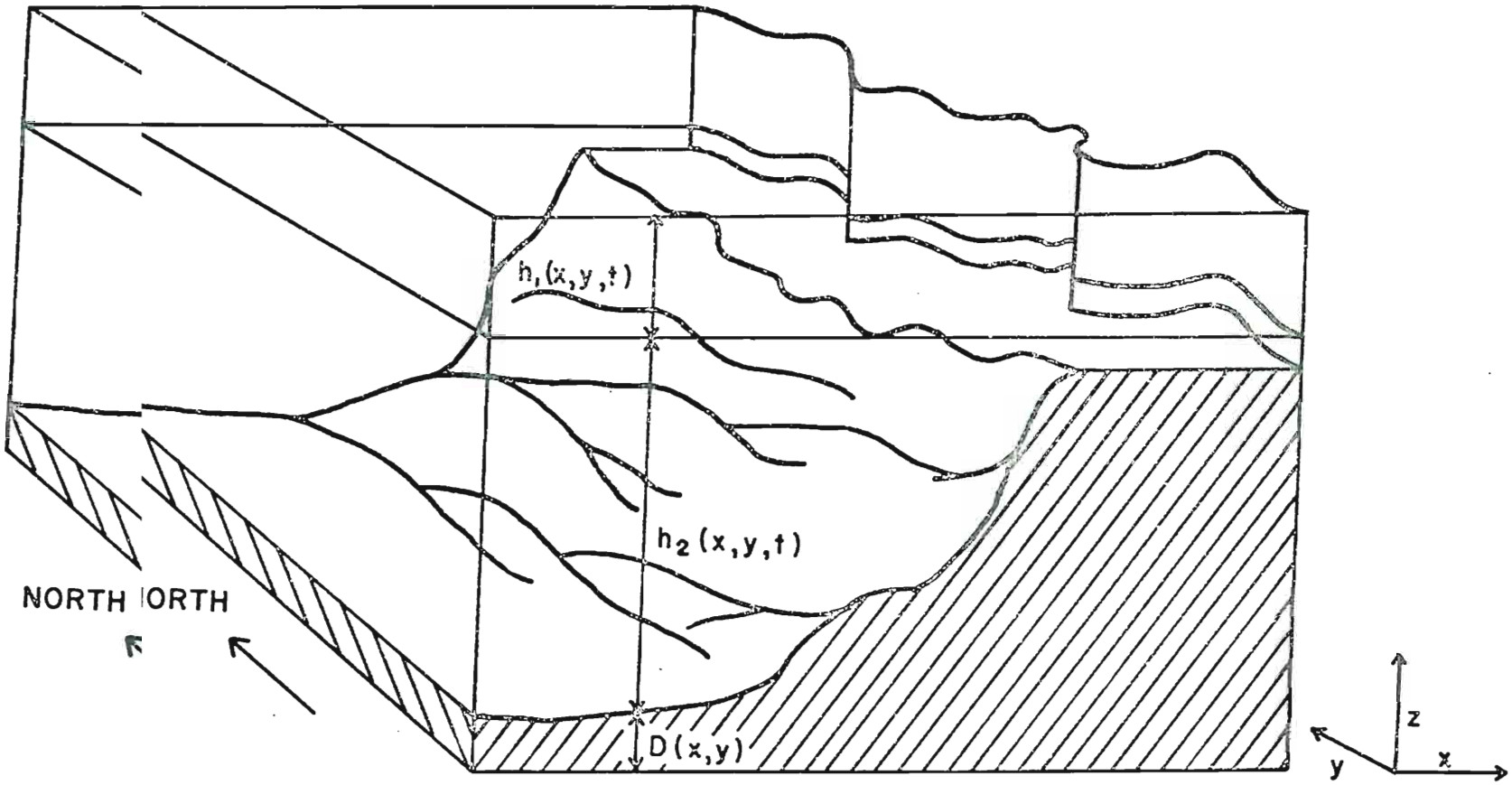

Fig. 1. Geometry of the x-y-t, two-layer model. The coastline is y-depen-dependent. The layer thicknesses h_1 and h_2 are dependent on x,y, and t (the frthe free surface and layer interface are shown here as flat surfaces for purposeurpose of figure clarity). D(x,y) is the height of the bottom above an arbitrarbitrary reference level. Notice that the layer interface does not intersect thect the sloping topography.

b. Problem formulation

The ocean is modeled using a two-layer incompressible fluid assumed to be hydrostatic and Boussinesq. The effects of atmospheric pressure gradients and tides are neglected.

Layer densities ρ_1 and ρ_2 are constants. Thermodynamics and thermohaline mixing are not included. Implicit in these omissions is the assumption that the time scale for vertical advection will be much less than that for vertical eddy diffusion. This assumption is not very realistic, especially under conditions of strong surface turbulence, tidal mixing or shear instability. There is observational evidence that, in the Oregon coastal upwelling region, periods of shear instability do occur, with Richardson numbers < 10 having often been observed (Huyer, 1974). In a numerical model incorporating thermodynamics, Thompson (1974) has shown that vertical mixing may be comparable to vertical advection during the week to ten-day upwelling cycle.

Although the omission of thermodynamics precludes the evolution of a realistic steady-state, the present model has much to offer, especially owing to the transient nature of the upwelling event cycle. For small interface displacements, Thompson (1974) found good agreement between a purely hydrodynamic model and one with thermodynamics. All of the cases to be discussed below have maximum interface displace-

cases to be discussed below have maximum interface displace-

ments less than 30 m. Since a 50 m initial upper layer thickness is used in each case, this means the interface

is always at least 20 m from the surface, thus reducing inaccuracies due to neglect of thermodynamics.

Under the above assumptions the model equations are the vertically-integrated primitive equations for a rotating, stably stratified fluid on a β-plane (Hurlburt, 1974).

$$\frac{\partial \vec{V}_1}{\partial t} + \vec{V}_1 \cdot \nabla \vec{V}_1 + \hat{k} \times f\vec{V}_1 = -g\nabla (h_1 + h_2 + D) + \frac{\vec{\tau}_s - \vec{\tau}_I}{\rho_1 h_1} + A\nabla^2 \vec{V}_1 \tag{1}$$

$$\frac{\partial h_1}{\partial t} + \nabla \cdot (h_1 \vec{V}_1) = 0 \tag{2}$$

$$\frac{\partial \vec{V}_2}{\partial t} + \vec{V}_2 \cdot \nabla \vec{V}_2 + \hat{k} \times f\vec{V}_2 = -g\nabla (h_1 + h_2 + D) + g'\nabla h_1 + \frac{\vec{\tau}_I - \vec{\tau}_B}{\rho_2 h_2} + A\nabla^2 \vec{V}_2 \tag{3}$$

$$\frac{\partial h_2}{\partial t} + \nabla \cdot (h_2 \vec{V}_2) = 0 \tag{4}$$

where 1 denotes the upper layer, 2 the lower layer,

$$\begin{aligned}
\nabla &= \frac{\partial}{\partial x}\hat{i} + \frac{\partial}{\partial y}\hat{j} \\
\vec{V}_i &= u_i \hat{i} + v_i \hat{j} \\
f &= f_0 + \beta (y - y_0) \\
g' &= g(\rho_2 - \rho_1)/\rho_2 \\
\vec{\tau}_s &= \tau_{sx}\hat{i} + \tau_{sy}\hat{j} \\
\vec{\tau}_I &= \rho C_I |\vec{V}_1 - \vec{V}_2| (\vec{V}_1 - \vec{V}_2) \\
\vec{\tau}_B &= \rho C_B |\vec{V}_2| \vec{V}_2
\end{aligned} \tag{5}$$

and i = 1, 2. Symbols are defined in the Appendix. Derivation of the layered equations and explanation of the interfacial and bottom stress formulations can be found in O'Brien and Hurlburt (1972).

No-slip conditions apply at the eastern and western boundaries. Northern and southern boundary conditions are the quasi-symmetric boundary conditions described by Hurlburt (1974). These open-basin conditions are particularly suited to our purposes. We are interested in modeling the upwelling circulation of the Oregon shelf region, a region of approximately 500 km N-S extent. To model such a region adequately with a closed basin, it would be necessary for the basin's horizontal dimensions to be O(1000 km) for, as shown by Hurlburt and Thompson (1973), a Sverdrup interior will not develop in a closed basin of lesser dimensions. A Sverdrup interior is, however, one of the primary dynamical features of the upwelling circulation and must be preserved. Use of the quasi-symmetric boundary condition allows us, with relative economy, to solve the problem in an open basin of mesoscale N-S extent and still develop a Sverdrup interior in the model.

Initial conditions for the model cases to be described in Section 4 are either (i) rest or (ii) the quasi-balanced initial state prescribed by Hurlburt (1974). The quasi-balanced initialization filters out the inertial oscillations, Rossby waves, and gravity waves caused by impulsive application of the wind stress at t = 0, allowing an easier interpretation of the low frequency dynamics. In comparisons

between cases started from rest and from a quasi-balanced state, Hurlburt (1974) found that the amplitude of external gravity waves excited by the impulsive application of the wind stress were reduced up to three orders of magnitude in the quasi-balanced initial state cases, without significant effect on low frequency aspects of the solutions.

The parameter space of the model is explained by Hurlburt (1974). We explain the specific choice of parameters for the Oregon upwelling case in Sections 3 and 4. Eqs. (1) - (4) with the specified boundary and initial conditions and parameters close the problem. The non-linear nature of the model equations, and the arbitrary bottom topography and coastline require a numerical approach to the problem.

c. Numerical scheme

The numerical model devised by Hurlburt (1974) employs the efficient semi-implicit scheme described by O'Brien and Hurlburt (1972) in the x direction; an explicit scheme is used in the y direction. Diffusive terms are treated implicitly in the x direction using the Crank-Nicholson (1947) scheme. Other frictional terms are lagged in time. Leap-frog time differencing is used for Coriolis and non-linear terms. Advective terms are approximated using Scheme F from Grammeltvedt (1969). The model uses a variable resolution grid: discrete variations in the x direction and an analvti-

Grammeltvedt (1969). The model uses a variable resolution grid: discrete variations in the x direction and an analyti-

cally stretched variable in the y direction. In the present

work, the stretching option in y was not used, Δy being constant and equal to 10 km. Table 1 describes the discrete variation of Δx as a function of x. This grid was used for all model cases discussed hereing.

Table 1

Δx vs. x

Mesh boundaries in km from easternmost point of ocean extent	Δx in km
0	
	4
72	
	8
88	
	20
148	
	50
298	
	101
500	
	300
5000	

To model the coastal upwelling circulation correctly, the zonal extent of the basin must be great enough to admit a Sverdrup interior, i.e., O(1000 km). Also, the grid resolution in the eastern ocean must be fine enough to resolve boundary layer phenomena and the topographic forcing ($\Delta x < 5$ km). In an x-y model without a variable grid, this problem would be prohibitively expensive, requiring five

problem would be prohibitively expensive, requiring five

times as many grid points. A coarse grid has been used in the western ocean since we are not interested in the solution

there. Hurlburt and Thompson (1973) and Hurlburt (1974) have demonstrated that for a simple equatorward wind stress in the upwelling area, the solution for the eastern ocean is independent of that for the western boundary region provided the zonal extent of the model is great enough to admit a Sverdrup interior. Discrete variation in x also allows the advantage of using the same value of Δx over all parts of a variable coastline.

Economic considerations are extremely important in numerical modeling of the upwelling circulation. Once the size of the region to be modeled and the time period of interest is determined, one seeks, for economy, the largest time step compatible with numerical stability and the purposes of the study. Since we use an explicit scheme in the y-direction, the most severe constraint on the permissible time step is given by the Courant-Friedrichs-Lewy (CFL) linear stability condition

$$\Delta t \leq \min \Delta y/(g \cdot \max (H_1 + H_2))^{1/2} \qquad (6)$$

which essentially says that the time step must be small enough so that during that time step the fastest moving wave in the system will not travel a distance larger than the smallest spatial grid increment. For our problem the fastest wave is the external gravity wave whose speed is $(g \cdot \max (H_1 + H_2))^{1/2}$. Fine resolution of the longshore
fastest wave is the external gravity wave whose speed is $(g \cdot \max (H_1 + H_2))^{1/2}$. Fine resolution of the longshore scales, i.e., small Δy, and a realistically deep basin, i.e.,

large max $(H_1 + H_2)$ are both desired. Thus the CFL condition forces a compromise between economy and fine resolution of longshore scales and to a lesser extent, puts a practical limit on the total basin depth. These constraints directly affect the design of the present experiment as discussed in Sections 3 and 4.

3. BOTTOM TOPOGRAPHY AND COASTLINE

Our intent is to put the Oregon bottom topography and coastline into the Hurlburt (1974) model and to study the resulting effects on the coastal upwelling circulation. The region of primary interest is the Oregon shelf, although, as noted by Huyer (1974), the northeastern Pacific coastal upwelling region stretches from Vancouver Island to Baja California.

The necessary bathymetry data D(x,y) were digitized from the 1968 Coast and Geodetic Survey charts 1308N-17 and 1308N-22 and from a chart compiled by Dr. John V. Byrne from unpublished Coast and Geodetic Survey soundings (personal communication). The data were digitized on a grid of 500 km N-S extent and 120 km E-W extent using a 2 km grid spacing in N-S and E-W. The northern and southern limits of the digitized data are approximately 46°30'N and 42°N (Fig. 2). The digitized region includes the entire N-S extent of the Oregon coastline, plus a small segment north of the Columbia River. In the digitization process the coastline was extrapolated across the mouths of all rivers and bays. There is no river input into the model. Also, the coastline was constrained to be a single-valued function of latitude.

and bays. There is no river input into the model. Also, the coastline was constrained to be a single-valued function of latitude.

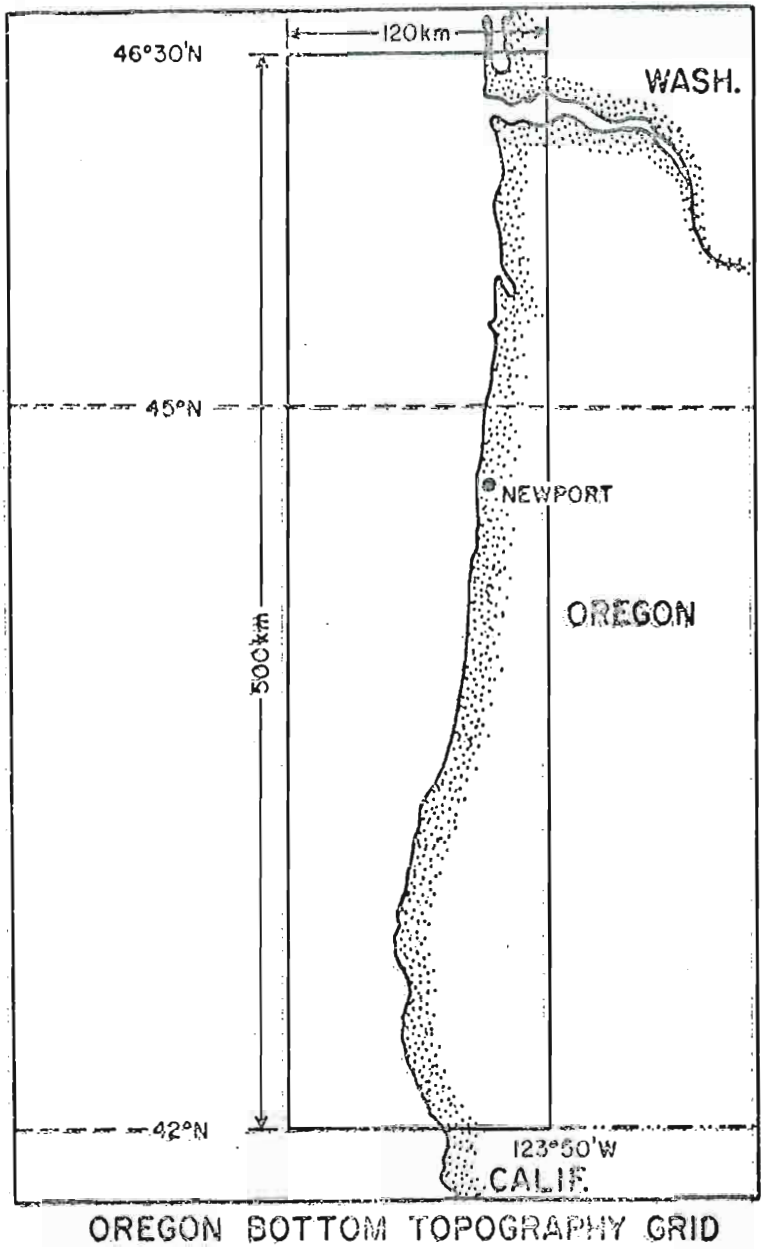

Fig. 2. The Oregon bottom topography data grid. The solid line bounds the ocean region for which the bottom depths were digitized on a 2 km grid.

Fig. 2. The Oregon bottom topography data grid. The solid line bounds the ocean region for which the bottom depths were digitized on a 2 km grid.

The chart data are bottom depths in meters below mean lower low water. Points falling in areas of depth 1000 m or greater were arbitrarily assigned the value 1000 m. During the digitization phase, we felt that this depth was a reasonable upper limit on basin depth for the purposes of our study. The error for depths $\leq$ 1000 m is estimated to be, at most, $\pm$ 5% (Peffley, 1974). As explained in Section 4, we chose a basin depth of 400 m for our model runs. Fig. 3 shows a computer contouring of the digitized bathymetry data described above. Since our model basin depth is 400 m, we have only shown isobaths as deep as 400 m.

A quick look at the almost meridional Oregon coastline gives the deceptively appealing impression of geometric simplicity. Bathymetric charts such as Fig. 3 however, reveal a complexity in the topography which will obviously make it more difficult to understand the observed ocean circulation. The most prominent coastline feature is Cape Blanco, north of which is an essentially meridional coast. Underwater topographic features include the small width-scale O(10 km) Columbia River canyon (y = 225 in Fig. 3) and a much larger scale canyon (axis at y = 120 in Fig. 3). Another important part of the topography is a ridge system comprised of Stonewall and Heceta Banks (y = 40 to y = -40 in Fig. 3).

Shelf widths in the region shown in Fig. 3 vary from $\sim$15 km off Cape Sebastian (y = -212) to $\sim$ 70 km for the area

Shelf widths in the region shown in Fig. 3 vary from $\sim$15 km off Cape Sebastian (y = -212) to $\sim$ 70 km for the area just south of the Columbia River canyon (y = 225) and the

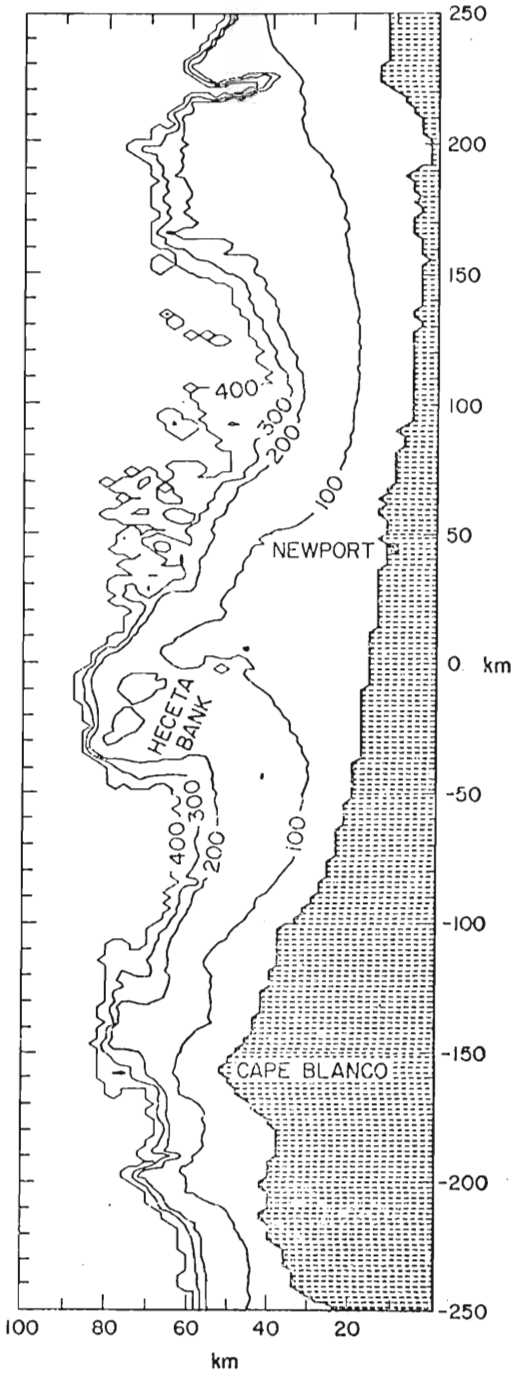

Fig. 3. Bathymetric chart of the Oregon coastal region contoured by computer from the 2 km grid digitized bottom topography data. Depths are in meters. Isobaths deeper than 400 m are not shown. Ordinate labels correspond directly to those of the x-y plots in subsequent sections. Althouth a right-handed coordinate system is used, positive abscissa values are used in this and other x-y plots for simplicity. References in the text to positions in x-y plots imply km.

area of Heceta Bank. Off Heceta Bank, the shelf edge may be in water as shallow as 100 m, while the shelf break off Cape Blanco is in much deeper water, O(300 m).

The magnitudes of the shelf slope and continental slope show considerable longshore variability. Smallest shelf-slopes are in the Heceta Bank region, $O(2\times10^{-3})$; largest shelf-slope values $O(1.5\times10^{-2})$ occur on that portion of the shelf between Cape Blanco and Cape Sebastian. Continental-slope values are smallest in the area off Cascade Head ($y = 90$) where they are $O(1.5\times10^{-2})$, compared with order of magnitude greater slopes found seaward of the shelf edge off Heceta Bank. Local zonal bottom height gradients range from $-.9\times10^{-1}$ to 1.8×10^{-1}; local meridional bottom height gradients range from -1.8×10^{-1} to 1.5×10^{-1}. Another important statistic for the Oregon shelf is the absolute zonal location of the shelf edge. Using the easternmost position of the shore in Fig. 3 as a reference, the shelf break can be as far west as 75 km (off Heceta Bank), or as close as 30 km (off Cascade Head). It is apparent that the ocean bottom off Oregon exhibits considerable longshore diversity; it also presents considerable problems to the numerical modeler. Practical limitations made it impossible for us to resolve the steep slopes of the continental-slope region and the large magnitude slopes associated with small-scale features.

the steep slopes of the continental-slope region and the large magnitude slopes associated with small-scale features.

To determine the important scales of variability in the bottom topography, a Fourier analysis of the zonal rows

of the digitized bottom heights was done. It showed that for practically every row, at least 90% of the variance in bottom heights is in scales $\geq$ 8 km. A Fourier analysis of zonal position of the isobaths as a function of latitude showed that at least 90% of the variance is in scales $\geq$ 30 km. The zonal position of the coastline was similarly analyzed. Over 90% of the variance in coastal position was accounted for by scales $\geq$ 20 km.

Design of the numerical model grid was a compromise between availability of computer resources and the need for resolution of the most important scales. We attempted to use resolution fine enough to resolve both the forcing functions and the dependent variable fields in the important coastal region. Theory indicates that the important onshore-offshore scales for the upwelling circulation are the shelf width L_s and the baroclinic radius of deformation λ_I. For a two-layer model

$$\lambda_I = \left[\frac{g' h_1 h_2}{f^2(h_1+h_2)}\right]^{1/2} \qquad (7)$$

where h_1 and h_2 are the time-dependent upper and lower layer thicknesses. Taking representative valus for the Oregon shelf: $g' = 2\times10^{-2}$ m sec^{-2}, $f = 10^{-4}$ sec^{-1}, $h_1 = 50$ m, and $h_2 = 150$ m we get $\lambda_I \simeq 9$ km. As an aside, the relative scales of the shelf width and the radius of deformation are $h_2 = 150$ m we get $\lambda_I \simeq 9$ km. As an aside, the relative scales of the shelf width and the radius of deformation are of interest, for as noted by Mooers and Allen (1973), the upwelling problem case in which $L_s \leq \lambda_I$ is not understood.

Much of the present theory assumes $L_s >> \lambda_I$. Since there are regions of the Oregon shelf where $L_s \simeq 15$ km, we must be careful in applying theoretical results based on the assumption $L_s >> \lambda_I$.

In choosing the zonal resolution we needed to use a Δx at least small enough to resolve the features governed by the baroclinic radius, i.e., $\Delta x \simeq 5$ km. If the most important zonal scales of topographic or wind stress forcing were smaller than the baroclinic radius of deformation, the need for a smaller Δx would be implied. We have used Δx = 4 km within the 70 km nearest the coast. As can be seen by comparing Table I and Fig. 5, the model region in which Δx = 4 km is wide enough to include almost all the sloping topography.

Longshore scales of the upwelling and current fields are determined primarily by the scales of the forcing functions. In recent work Pedlosky (1974a) has analyzed the role of the longshore structure of the wind stress in coastal upwelling. He concluded: "The long-shore currents are dominated by the largest scales of forcing, while the onshore and upwelling flow is sensitive to all scales of forcing with their structure a strong function of scale." The two forcing functions in the model cases presented below are a y-independent wind stress and the coastline-bottom topography configuration. Thus, we based our choice of Δy on the meridional Fourier analysis of the coastline position and

the bottom heights. Since at least 90% of the longshore variability is in scales $\geq$ 20 km, we chose Δy = 10 km for the model cases discussed below. A smaller Δy, although desirable, was not within the economic constrains of the study. Halving Δy doubles the number of grid points and, due to (6), also halves the allowable time step, thus resulting in a four-fold increase in cost.

A smooth representation of the coastline, ignoring features with scales $\leq$ 20 km, was chosen for use in the model grid. The coastline used is depicted in Fig. 4. Notice that the 500 km region of Fig. 3 has been extended by adding two regions of y-independent coastline, 150 km in the north and 150 km in the south. The zonal portion of the coast in the northern region is a simple repetition of its position at y = 250 km, and likewise that in the southern region is a repetition of the coastal position at y = -250 km. The topography between y = 250 and y = -250 in Fig. 4a was chosen as every fifth row of the bathymetry data shown in Fig. 3. Y-independent extensions of the isobaths into the north and south regions were made in a manner exactly similar to that described for the coastline. These regions of y-independent coastline and topography are used to reduce longshore derivatives of the velocity field near the northern and southern boundaries. The open-basin boundary conditions are based on the assumption that these derivatives will be small.

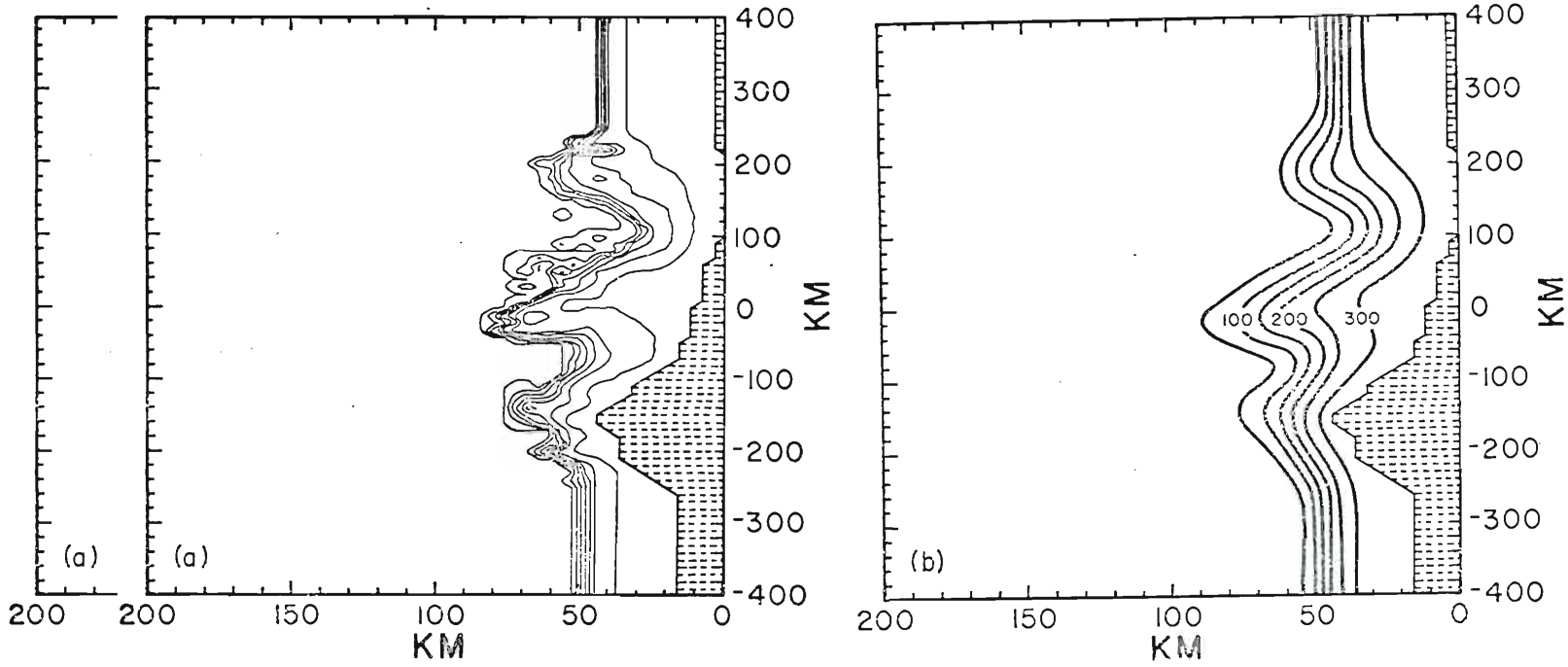

Fig. 4. (a) Unsmoothed contours of bottom height shown on the model grid. Total ſotal depth of the basin is 400 m. The westernmost height contour is at 50 m; the easterɐasternmost is at 300 m. The maximum height of the topography is 345 m. Notice the lathe lack of y dependence in the bottom topography and coastline in the northern-most lnost 150 km and southernmost 150 km of the grid. The full 800 km N-S extent of the mothe model region is shown here. Although the total basin width is 5000 km, only the pathe part within 200 km of the coast is shown in this and subsequent figures, this bthis being the region of greatest interest. (b) Smoothed bottom topography heights in m oin m obtained by smoothing the topography of Fig. 4a as explained in the text. This fſhis figure shows the coastline used in all model cases discussed herein, and the topogrtopography used in all cases discussed except the flat bottom cases. The maximum heightɪeight of the bottom is 345 m.

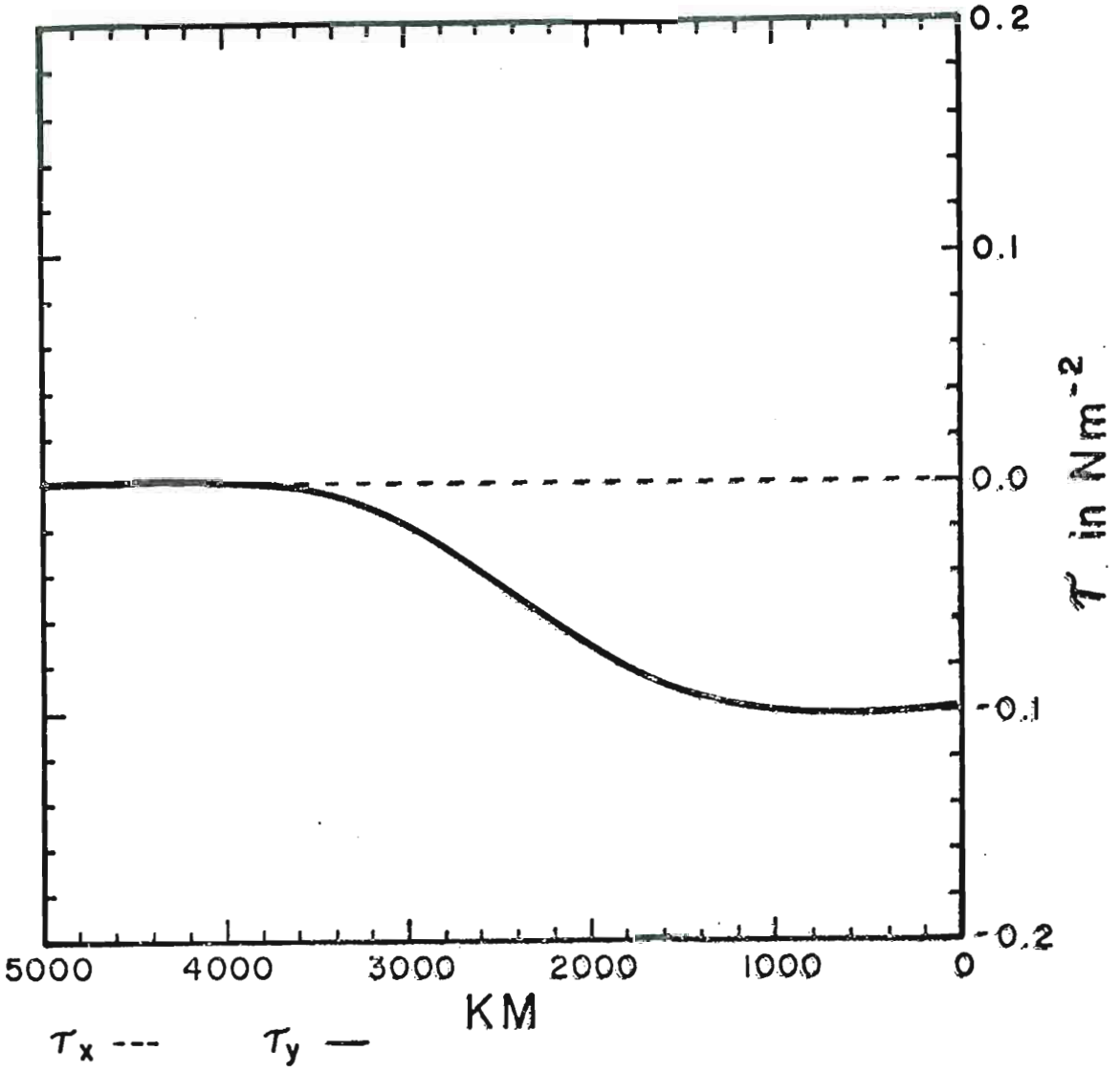

Fig. 5. E-W profile of the y-independent, time-independent wind stress used in all spin-up cases described herein. The x component of the wind stress is zero everywhere.

The topography shown in Fig. 4a produced severe instabilities in the model solutions. The steep slopes present in the actual topography demand extremely fine resolution, finer than was economically feasible in this study. Thus we chose to smooth the topography of Fig. 4a. The following filter was used: (i) a nine-point smoother designed to eliminate identically $2\Delta x$ and $2\Delta y$ variation was applied four times to the bottom height field, (ii) a Hanning filter ($X_j = .5X_j + .25(X_{j-1} + X_{j+1})$) was applied twelve times to the meridional rows of the bottom height field. More severe smoothing was required in the y direction due to the coarser resolution in y. The smoothed topography is shown in Fig. 4b. All model cases discussed, except the flat bottom cases, used this topography.

If we compare the zonal position of the coastline in Fig. 4b to that of the actual coast, we find an absolute error with mean of 1.3 km and standard deviation of 1.2 km. Comparing the bottom topography heights of Fig. 4b with those of Fig. 3 shows an absolute error of mean 10.3 m and standard deviation of 23.7 m. The extreme slopes of the actual topography have been smoothed out. The range of local zonal bottom height gradients for the smoothed topography is from zero to 1.9×10^{-2}. Local meridional height gradients range from -3×10^{-3} to 3×10^{-3}. Although quantitative aspects of the bottom and coastline configuration

gradients range from -3×10^{-3} to 3×10^{-3}. Although quantitative aspects of the bottom and coastline configuration

have been distorted, we have attempted to use a smoothing

scheme which preserves both the qualitative aspects and the most important quantitative scales.

4. CASE DESCRIPTIONS

We will now define the specific model parameter space used for the Oregon cases, and describe the structure of these separate cases, the results of which are discussed in Sections 5 and 6. We attempted to choose model parameters which agree with observations in the Oregon coastal upwelling area. The parameter values (common to all cases to be discussed) are given in Table 2.

Since our interest is in modeling the circulation on the shelf and not abyssal currents we have chosen to use a maximum basin depth of 400 m. This assumption is not a severe one, for observations (Mooers et al., 1975) indicate that the upwelling circulation is confined to the upper few hundred meters off the Oregon coast. Also, Thompson (1974) has found no significant qualitative differences in comparing the results of upwelling models with basin depths O(200 m) to those from model runs using much deeper basins.

In this study, we model the permanent pycnocline with the layer interface, and model upwelling by displacements of that interface from its initial position. If the convention of using the 25.5 - 26.0 σ_t band to specify the permanent pycnocline is used, observations show that σ_t surface to be

of using the 25.5 - 26.0 σ_t band to specify the permanent pycnocline is used, observations show that σ_t surface to be

at a depth of 50 - 100 m off Oregon in the early summer.

Table 2

Model parameters

Parameter	Symbol	Value
E-W basin extent	L_x	5000 km
N-S basin extent	L_y	800 km
Inital upper layer thickness	H_1	50 m
Initial lower layer thickness	H_2	variable
Maximum total basin depth	$\max(H_1+H_2)$	400 m
Coriolis parameter at y = 0 (latitude 44°15')	f_0	1.02×10^{-4} sec^{-1}
df/dy	β	2×10^{-11} m^{-1} sec^{-1}
Gravitational acceleration	g	9.80 m sec^{-2}
Reduced gravity	g'	2×10^{-2} m sec^{-2}
Horizontal eddy viscosity coefficient	A	5×10^{2} m^2 sec^{-1}
Upper layer density	ρ_1	1.000×10^{3} kg m^{-3}
Lower layer density	ρ_2	1.002×10^{3} kg m^{-3}
Interfacial frictional drag coefficient	C_I	10^{-5}
Bottom frictional drag coefficient	C_B	10^{-3}
Time step	Δt	120 sec
Grid increment in x direction	Δx	see Table 1
Grid increment in y direction	Δy	10 km

It will be remembered that in the model the interface is not allowed to intersect the topography. In order to include more of the shelf topography, we have chosen the initial depth of the interface to be 50 m. As indicated in Fig. 1, the topography is everywhere at least 5 m below the initial interface position. A density difference of 2 kg m^{-3} is used to approximate that between the upper wind-mixed layer and lower layer. This value agrees with typical Oregon observations, e.g., Huyer (1974).

We have chosen a value of the eddy viscosity, A, different from that used in several previous numerical studies of upwelling, e.g., O'Brien and Hurlburt (1972), Hurlburt and Thompson (1973). These authors used $A = 10^2$ m^2 sec^{-1}. However, the bottom topography of the present study is much more irregular than any previously used, thus it is more apt to induce instabilities. We found the stability of our solutions to be much improved using a value of $A = 5\times10^2$ m^2 sec^{-1}. Values of this magnitude are consistent with observations; Stevenson et al. (1974) have estimated A as high as 2.1×10^3 m^2 sec^{-1} for the CUE-I experimental region.

As in Hurlburt (1974), in the northern and southern boundary conditions, the N-S pressure gradient at the western boundary has been set to zero. More realistically, an integral constraint should be employed to determine the N-S

tegral constraint should be employed to determine the N-S
pressure gradient at $x = -L_x$. Recently, this has been done, and results for the eastern ocean are unaffected (Hurlburt

and Thompson, personal communication). Following Thompson and O'Brien (1973) we choose $C_I = 1\times10^{-3}$ and $C_B = 1\times10^{-5}$. However, it should be noted that, as shown by Thompson and O'Brien (1973), the solutions for the upwelling area are relatively insensitive to the choice of C_I and C_B. The choice of Δt is determined by (6). We used a value ≈ 80% of that permitted by the CFL constraint. The range of values for the Coriolis parameter is from $.95\times10^{-4}$ sec^{-1} at the southern boundary to 1.11×10^{-4} sec^{-1} at the northern boundary.

The wind stress used is shown in Fig. 5; τ_{sx} is zero everywhere; τ_{sy} is y-independent and time-independent and constant over the 800 km nearest the coast. A simple wind stress with zero curl in the upwelling region was chosen to simplify interpretation of the Ekman dynamics. The maximum of $|curl_z \tau_{sy}|$ is 6×10^{-8} N m^{-3} at a distance of 2450 km offshore. The magnitude of τ_{sy} in the upwelling area agrees with observations in the CUE-II experiment area, e.g., Halpern (1974).

Three model cases will be discussed. Case I used the coastline of Fig. 4b, but with a flat bottom, depth 400 m, and was started from rest. Case II used the topography and coastline of Fig. 4b and was also started from rest. Case III used the topography and coastline of Fig. 4b, but was started from the quasi-balanced initial state discussed in Section 2. Each of these cases was driven for 5 days

with the wind stress shown in Fig. 5. Also, to study the relaxation of the upwelling, Cases I and II were repeated identically as described above except that the wind forcing was "shut off" at t = 2.5 days and the integration continued for another 2.5 days with zero wind stress. In the subsequent discussion, we will refer to the initial period with wind stress forcing as the "spin-up" period, and to the period with zero wind stress as the "spin-down". The wind forcing of the Oregon upwelling regime is highly variable and even changes direction during the upwelling season. Therefore, we feel that a study of the onset of upwelling and initial stages of decay is important to understanding the Oregon case.

5. SPIN-UP

a. Introduction

In this section, we will examine several features of the model circulation which develop during spin-up, and in Section 6, we will look at aspects of the spin-down solutions. The figures of Sections 5 and 6 are computer drawn contours (or vector plots) which depict graphically the numerical model solutions. With the exception of Figs. 7 and 19, the pictures are synoptic. The best Oregon observations are confined to a relatively small region and necessarily are only quasi-synoptic. Thus, these figures offer a unique opportunity for the theoretician and observer to visualize a three-dimensional simulation of the complex mesoscale Oregon upwelling circulation.

Analysis of the model solutions will emphasize the role of longshore variability of the bottom topography and the coastline. Comparisons with Oregon observations and predictions of theory will be made when possible as an aid to understanding the dynamics.

In general, in the figures of this section, the topography case started from the quasi-balanced state is presented in preference to that started from rest. The former allows
graphy case started from the quasi-balanced state is presented in preference to that started from rest. The former allows
a clearer analysis of the low frequency dynamics. All figures of Section 5 (except Figs. 7 and 13) are at day 5.

As an aid to understanding, the reader is encouraged to make a photocopy transparency of Fig. 4b to use as an overlay in interpreting the figures portraying topography case solutions.

As a review, we will describe the essential dynamics of coastal upwelling for a β-plane case with equatorward wind stress, a meridional coastline and a flat bottom. The longshore flow is nearly geostrophic. A Sverdrup balance exists in the interior. Offshore flow in the upper layer is Ekman drift reduced by a longshore pressure gradient; u_2 the onshore flow in the lower layer is geostrophic. Near the coast, the zonal flow must go to zero to satisfy the boundary condition, and geostrophy breaks down resulting in an equatorward jet in the upper layer and a poleward jet in the lower layer.

The longshore pressure gradient reduces the barotropic mode near the coast and permits the poleward undercurrent to develop. The cause of the longshore pressure gradient has been a subject of controversy. Hurlburt and Thompson (1973) considered an x-z model which neglected y derivatives except those of the pressure gradient terms and the Coriolis parameter. By comparing the upper layer y-momentum equation to the zonally-integrated upper layer vorticity equation, they derived the result

$$\int_{-L_x}^{x} \beta v_1 \, dx = g \frac{\partial}{\partial y} (h_1 + h_2 + D)\Big|_{x} - g \frac{\partial}{\partial y} (h_1 + h_2 + D)\Big|_{-L_x} \qquad (8)$$

which shows how a N-S sea surface slope can be induced by the β effect.

When variable topography is considered, the situation becomes more complex, and as was noted by Sarkisyan and Ivanov (1971): " . . . the bottom relief competes successfully for significance with such an important factor as the β effect." Hurlburt (1974) listed three dynamical principles as likely to aid explanation of dynamics associated with longshore variations in topography: (1) conservation of potential vorticity, (2) topographic β effect (β_T effect) and (3) joint effect of baroclinicity and bottom relief. He found the β_T effect to be important dynamically, even for mesoscale features, O(100 km).

How β_T becomes important can be illustrated by considering a barotropic vorticity equation (Hurlburt, 1974)

$$\frac{\partial}{\partial t}\left(\frac{\partial v}{\partial x} - \frac{\partial u}{\partial y}\right) = - f\left(\frac{\partial u}{\partial x} + \frac{\partial v}{\partial y}\right) - \beta v + \frac{1}{\rho}\,\mathrm{curl}_Z\left(\frac{\vec{\tau}_s - \vec{\tau}_B}{h}\right) \quad (9)$$

where the advective terms and diffusive terms have been neglected. Substituting from the continuity equation

$$\left(\frac{\partial u}{\partial x} + \frac{\partial v}{\partial y}\right) = - \frac{1}{h}\left(\frac{\partial h}{\partial t} + u\,\frac{\partial h}{\partial x} + v\,\frac{\partial h}{\partial y}\right) \quad (10)$$

and defining

$$\beta_T = - \frac{f}{h}\,\frac{\partial h}{\partial y} \quad (11)$$

yields

$$\beta_T \qquad h\ \partial y$$

yields

$$\frac{\partial}{\partial t}\left(\frac{\partial v}{\partial x} - \frac{\partial u}{\partial y}\right) - \frac{f}{h}\left(\frac{\partial h}{\partial t} + u\,\frac{\partial h}{\partial x}\right) + (\beta_T + \beta)\,v = \frac{1}{\rho}\,\mathrm{curl}_Z\left(\frac{\vec{\tau}_s - \vec{\tau}_B}{h}\right) \quad (12)$$

Thus, the N-S sloping topography yields an analogous term to the planetary vorticity advection in the integral of Eq. (8), and can therefore exert an effect on the longshore pressure gradient.

Garvine (1974) has pointed out the importance of a realistic interior in coastal upwelling models. In the present study, the model interior approaches a Sverdrup balance

$$v_1 h_1 + v_2 h_2 = \frac{1}{\rho\beta} \text{curl}_z \vec{\tau}_s \qquad (13)$$

but does not achieve that balance by day 5. All cases exhibit barotropic Rossby waves. This is expected for the cases started from rest due to impulsive application of the wind stress curl. Even though the quasi-balanced state filters out wind stress induced Rossby waves in Case III, variations in depth and bottom stress, as in the right side of (9), still excite strong topographic Rossby waves. The role of these waves in the topographically induced barotropic flow is discussed in Section 5f.

b. Upwelling

Upwelling at day 5 for the flat bottom and topography cases is compared in Fig. 6. Quite striking is the longshore variability in the upwelling pattern for the case with topography compared to the flat bottom case. Generally weaker upwelling near the coast in the topography case is due to upwelling being induced further offshore by E-W bottom slope.

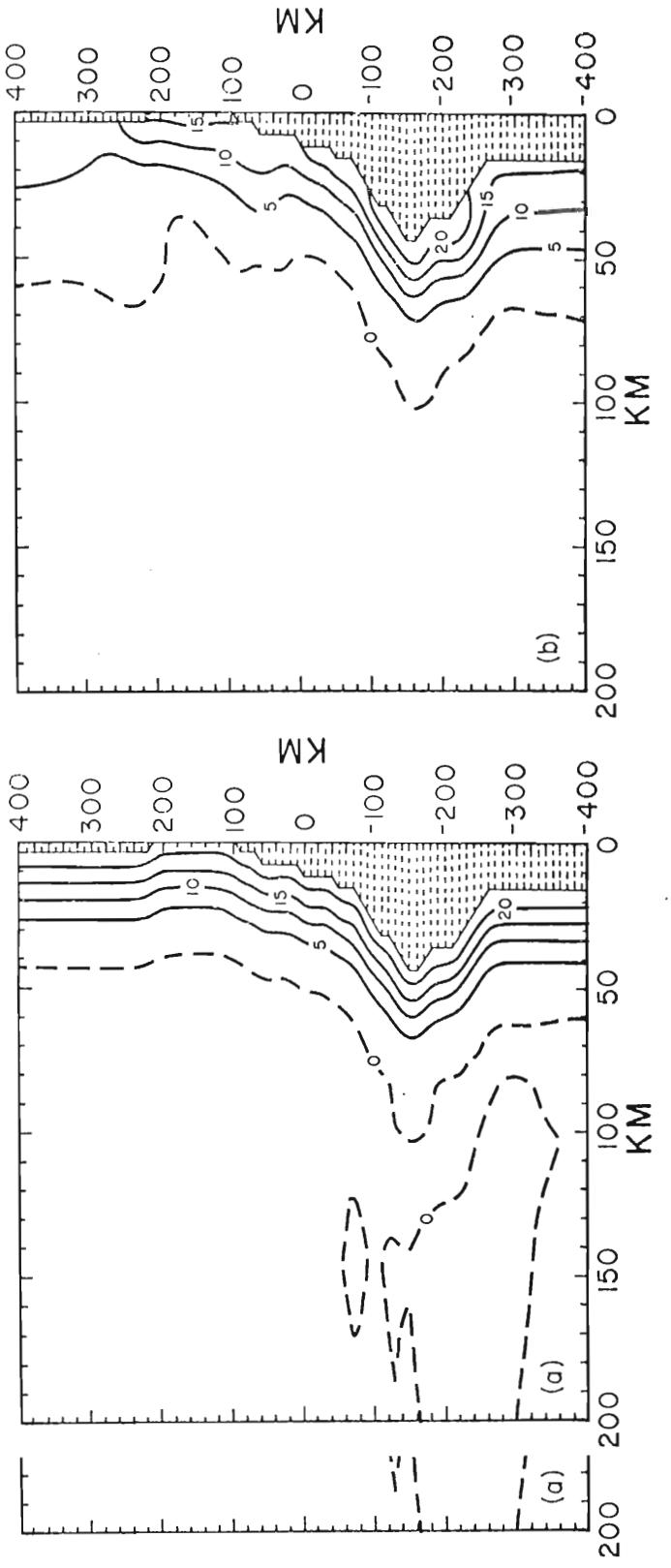

Fig. 6. Pycnocline height anomaly in m at day 5 for Case I in (a) and Caand Case III in (b). (Note that (a) and (b) identify the frames of the figurefigure.) The pycnocline height anomaly is the displacement of the layer interfinterface from its initial position of rest. In this, and subsequent figurefigures, positive contours are indicated by solid lines, the zero and negatinegative contours by dashed lines.

The layer interface of Case III exhibits vertical velocities at the coast of approximately 6×10^{-5} m sec^{-1} for the cape region and 4×10^{-5} m sec^{-1} for the CUE study area ($y \simeq 100$). Halpern (1973), estimating vertical velocities in the CUE area during two periods of southward winds, found values of 6.6×10^{-5} m sec^{-1} and 1.25×10^{-4} m sec^{-1}. Downwelling is seen in areas west of the zero contour.

Overlaying Fig. 6b with the topography transparency shows that favored areas of upwelling are the cape and the head of the mesoscale canyon (axis at y = 120). An interesting comparison can be made with Fig. 1 of Smith et al. (1971), a synoptic mapping of sea surface temperatures for a large part of the Oregon coast for a typical day of the coastal upwelling season. It shows pronounced upwelling south of Cape Blanco and another area of relatively strong upwelling between 44°40' and 45°20' (y = 50 to 120).

The intensity of upwelling shows an exponental decrease with distance offshore with an e-folding width roughly equal to λ_I, i.e., approximately 10 km. Studies of sea surface temperatures in the CUE-II area (y = 50 to 100) led Holladay and O'Brien (1975) to conclude that the mean isotherms tended to parallel isobaths. Due to the difference in scales, no very meaningful comparison can be made with Fig. 6b, except that for the mesoscale, the pattern of upwelling exhibits significant departures from the simple picture of upwelling paralleling the isobaths.

A decrease in the net vertical transport in the upwelling zone is observed with increase in latitude since the offshore Ekman transport is proportional to f^{-1}.

The role of coastline irregularities in influencing upwelling has been studied by Hurlburt (1974). For a flat bottom case with a cape roughly resembling that in the present study, he found: " . . . the upwelling follows the coastline, but otherwise this cape exhibits no dramatic effect on the pattern of vertical motion. Upwelling is greatest near the point of the cape and slightly greater on the southern side than on the northern side." This conclusion is borne out in Fig. 6a.

Several concepts shed light on explaining the pattern of longshore variation of upwelling in Fig. 6b. Shaffer (1974), in a study of coastal upwelling off NW Africa, observed that areas of cold water distribution marked heads of underwater canyons as geographically fixed centers of upwelling. Observations in that region showed lower level transport to be "funneled" along the axis of these (smaller scale) canyons.

Hurlburt (1974) studied effects of a symmetric mesoscale (half width $\sim$ 100 km) canyon on the upwelling pattern. He found: (1) decreased upwelling north of the canyon axis, (2) increased upwelling south of the axis and (3) enhanced upwelling on the axis near the shore. For a symmetric ridge,
(2) increased upwelling south of the axis and (3) enhanced upwelling on the axis near the shore. For a symmetric ridge, he found effects opposite to those of the canyon. Hurlburt

found these effects to be consistent with the β_T effect. In both cases, the dominant longshore scale appeared to be that of the topographic disturbance. Overlaying Fig. 6b, these basic results are seen to explain the observed pattern of upwelling. In particular, note enhanced upwelling south of the canyon (axis at y = 120) and at the coast near the canyon axis. Deflection of the zero contour at y = 180 (cf. flat case) is a persistent feature explained by the local "ridge canyon" system. The main ridge (axis at y = 0) and the canyon to the south act in the same manner to divert the height anomaly contours.

The relative importance of longshore coastline and topography variations is dramatically shown in Fig. 7, a comparison of y-t plots of upwelling at the coast for the flat and topography cases. Figs. 6b and 7b show that Cape Blanco is an area of greatly enhanced upwelling. But Fig. 7a clearly demonstrates that the coastline variation, i.e. the cape itself, is <u>not</u> the cause! We conclude that the relatively narrow shelf in the cape region does not "spread out" the upwelling in the offshore direction as happens along other parts of the shelf, thus forcing the upwelling to occur intensely in the region nearest the one-sided divergence. Fig. 7b also shows the main canyon to be a region of increased upwelling, with decreased upwelling associated with the adjoining ridges. Satellite photos (Meneely and Merritt, 1973) and airborne radiometer measurements (Elliot and O'Brien, 1975)

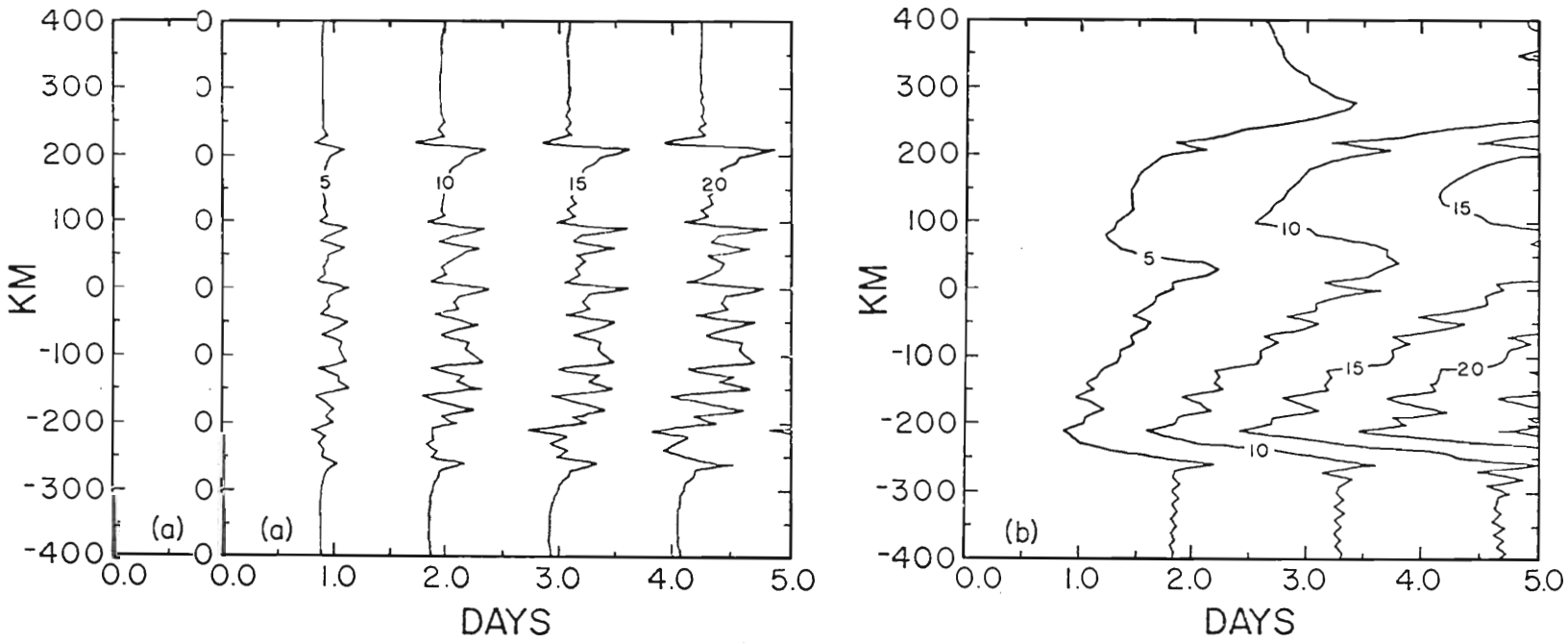

F Fig. 7. Contours of pycnocline height anomaly at the coast as a function of time time and N-S position for Case I in (a) and Case II in (b). Contours are labeled in m. m.

indicate that the region of Cascade Head (y = 85) is an area of relatively strong upwelling during the first days of southward winds, and Fig. 7b is in agreement.

We conclude by noting that the influence of topography is dominant over the coastline variations in determining the longshore pattern of upwelling for the Oregon coast.

c. Free surface

Fig. 8 compares the free surface anomaly for the flat bottom case to that of a case with topography. Except for the deflection due to coastline irregularities, Fig. 8a closely resembles the free surface for a β-plane case with flat bottom and a meridional coastline. Fig. 8b however is quite dissimilar, leading one to expect that topography exerts a strong influence on the free surface. A significantly greater depression of sea level occurs in the case with topography, part of which ($\sim$ 0.20 m in Case III) can be accounted for by lack of mass conservation in the numerical solution (0.05% of the original mass is lost by day 5). In the flat case mass loss amounts to approximately 0.0035 m of sea level change. Also, at t = 0 the sea surface in Case III is already depressed $\sim$ 0.13 m due to the quasi-balanced initialization. The remaining inter-case difference in free surface depression is attributed to a stronger barotropic mode induced by the topography. Ridging of the free surface near x = 115 is due to the topographic Rossby wave.

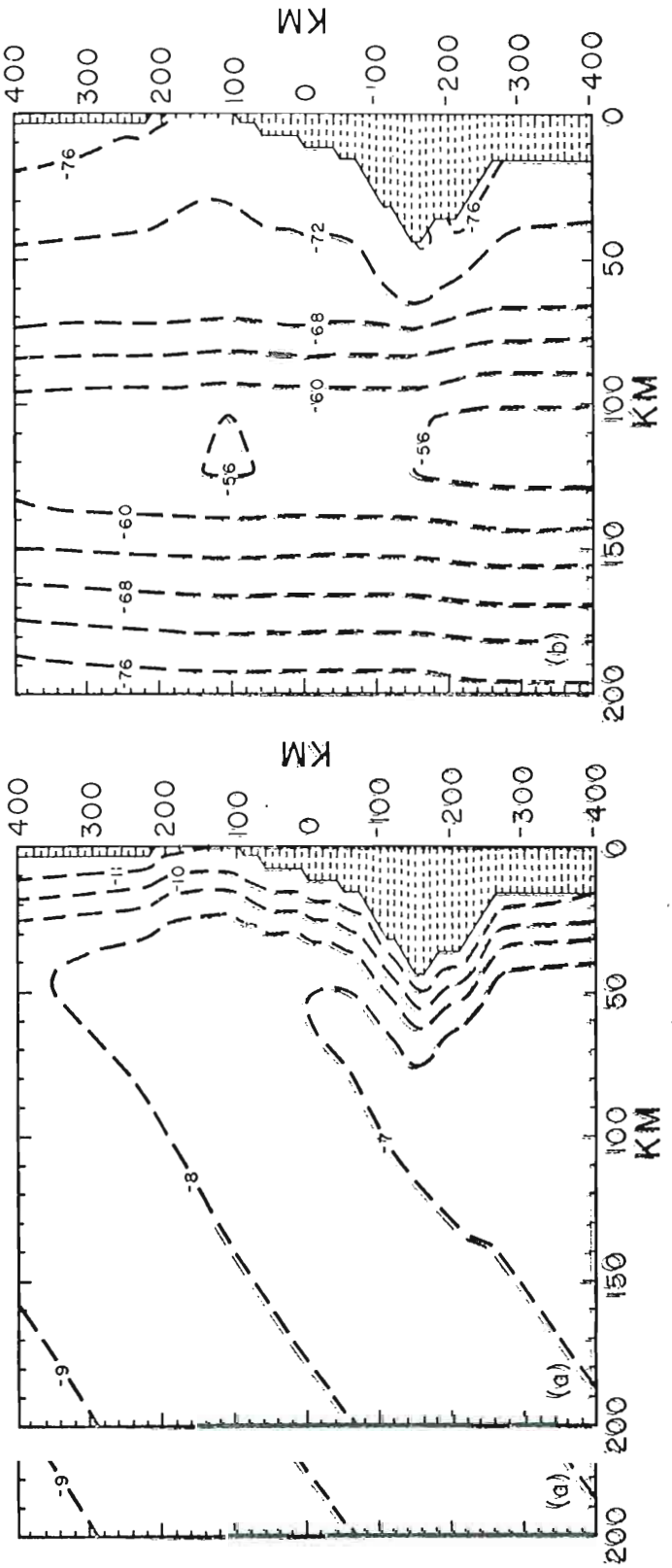

Fig. 8. Free surface anomaly ($m \times 10^{-2}$) at day 5 for Case I in (a) and Case IIase III in (b).

Observations at the Oregon coast (Mooers and Allen, 1973) indicate that barometrically adjusted sea level variations of 0.02 to 0.20 m can occur in a time scale of several days during an upwelling event. Brunson and Elliot (1974) found that the steric contribution to this fluctuation is 0.02 to 0.03 m. The residual is due to hydrodynamic effects and provides a base of comparison with the present study.

A N-S sea surface slope in the upwelling region (sloping downward toward the pole) is evident in both cases of Fig. 8, although more prominent in Fig. 8a. For the flat case, the slope is approximately $-.25\times10^{-7}$, or $-.25\times10^{-2}$ m per 100 km. Hurlburt (1974) found a N-S slope of approximately $-.57\times10^{-7}$ for a straight coast case with a 200 m deep basin. Each is in good agreement with theory (Hurlburt and Thompson, 1973) which predicts the N-S slope for a flat bottomed ocean to be

$$\frac{\tau_{sy}}{\rho g\ (h_1 + h_2)}$$

The sea surface slope in the upwelling zone of the topography case is more complex, and is not well delineated near shore in Fig. 8b, but is approximately $-.2\times10^{-7}$ for the outer shelf. A y-t plot of free surface anomaly at the coast for the flat case shows an interesting feature. The free surface drops to about -0.20 m at day 2.5 before relaxing to the level of Fig. 8a. During the five-day spin-up, the free surface at the south end of the basin drops faster

and rises slower than at the northern end, thus maintaining a relatively constant N-S slope. No such oscillatory feature is seen for the case with topography.

As discussed earlier, N-S sloping topography can introduce a term in Eq. (8) analogous to β and thus can affect the N-S sea surface slope. However, it is the zonal integral of βv_1 that is important, and Hurlburt and Thompson (1973) have shown that a basin width of O(1000 km) is necessary for the β effect to realistically affect the longshore pressure gradient. Values of β_T for the topography of Fig. 4b are large enough however (values of β_T of $\sim 1\times10^{-9}$ m^{-1} sec^{-1} are typical) to make the β_T effect important even on the mesoscale. Several regions of the actual Oregon bottom topography have β_T values $O(10^{-7}$ to 10^{-8} $m^{-1}sec^{-1})$. Thus, the topographic β effect is probably quite important in Oregon coastal upwelling circulation.

d. Upper layer flow

Figs. 9a and 9b show contours of the zonal* component of upper layer velocity for the flat bottom and topography cases. Although the flat case is relatively contaminated by

---

*The terms "zonal" and "onshore-offshore" are used interchangeably herein to mean motion in the x or E-W direction. Flow perpendicular to isobaths is referred to as "cross-isobath" flow. The terms "meridional" and "longshore" are used interchangeably to mean motion in the y or N-S direction. Flow parallel to isobaths is referred to as "along-isobath" flow. Huyer et al. (1975) found this convention for longshore flow to simplify the analysis of observational data without altering the qualitative results in any way.

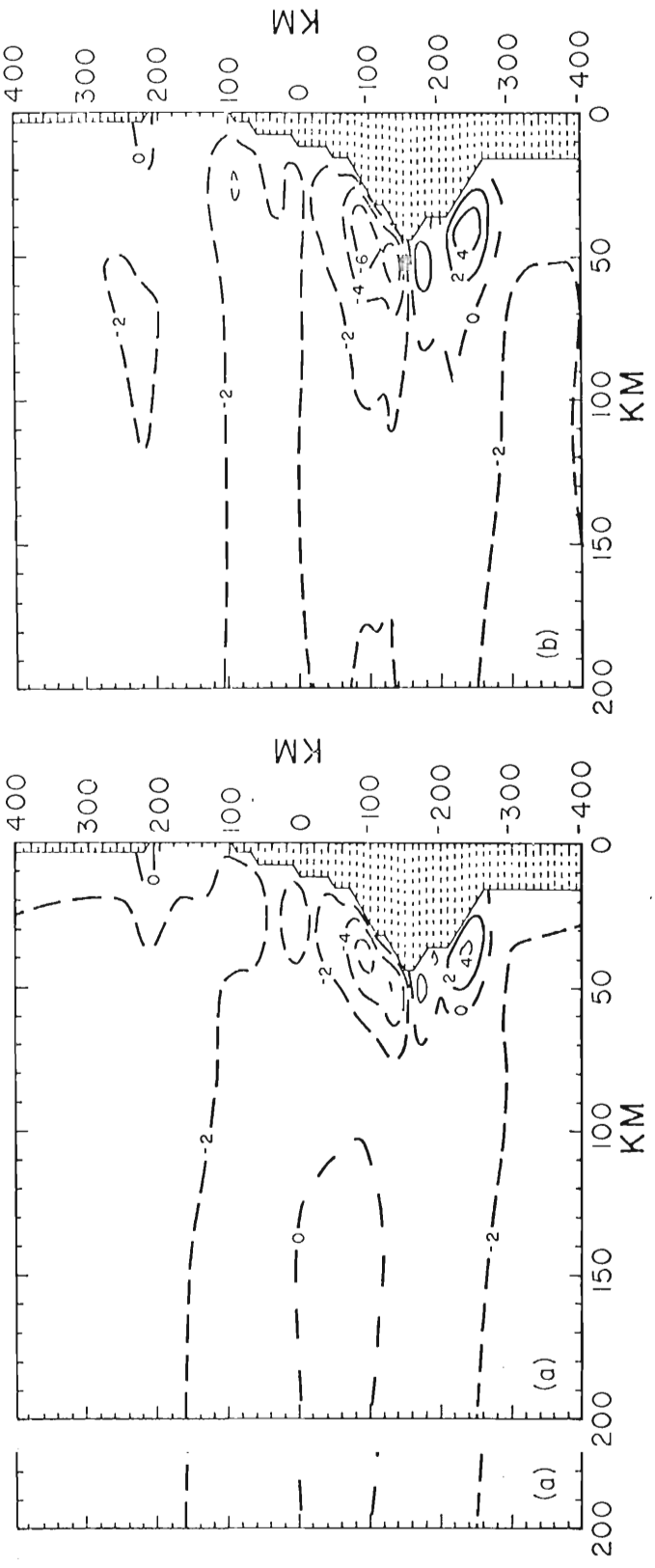
KM
400
300
200
100
0
-100
-200
-300
-400
0
50
100
150
200
KM
(b)
(a)
(a)

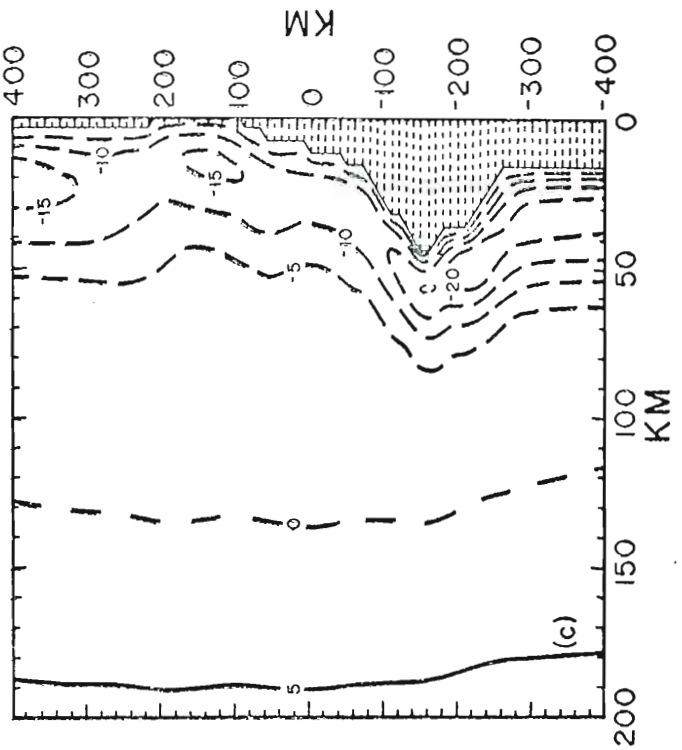

Fig. 9. Upper layer velocity components (m sec^{-1} x 10^{-2}) at day 5. Contoulontours of E-W component for Case I in (a) and Case III in (b). Contours of N-Sıf N-S component for Case III in (c).

inertial oscillations, the close qualitative similarity between Figs. 9a and 9b suggests the preliminary conclusion that topography has little effect on the upper layer zonal flow.

For an upper layer thickness of 50 m, Ekman dynamics predicts $u_1 = \tau_{sy}/(\rho_1 h_1 f)$ or $u_1 \simeq -0.02$ m sec^{-1}. Fig. 9a shows offshore speeds in good agreement with this. Mooers and Allen (1973) reported offshore velocities for the Oregon region to be 0.10 to 0.30 m sec^{-1} in the upper Ekman layer. According to Smith (1974) the surface Ekman layer is apparently restricted to the upper 20 m. Thus, the model predicts transports in good agreement with the observations, but the artificially thick upper layer of the model causes a decrease in zonal velocity.

The longshore dependence of u_1 appears to be dominated by coastline variations, and their associated length scales. Hurlburt (1974) has explained the existence of strong zonal flow along the relatively E-W portions of a coastline for the eastern ocean circulation.

Fig. 9c shows contours of the upper layer N-S component of velocity for the topography case. It is essentially similar to the flat bottom case (not shown) but exhibits a stronger poleward flow west of x = 120 in response to the barotropic mode of Fig. 8b. The equatorward surface jet in
stronger poleward flow west of x = 120 in response to the
barotropic mode of Fig. 8b. The equatorward surface jet in the topography case has somewhat greater longshore variability, and the jet maximum is slightly further offshore and

stronger than in the flat bottom case. O'Brien and Hurlburt (1972) first modeled the equatorward jet in an x-z, f-plane model explaining its existence in terms of conservation of potential vorticity.

The existence of the jet can also be understood in terms of upper layer momentum balance (Hurlburt and Thompson, 1973). Consider the linearized upper layer momentum equation, neglecting viscous terms

$$\frac{\partial v_1}{\partial t} + fu_1 = - g \frac{\partial}{\partial y} (h_1 + h_2 + D) + \frac{\tau_{sy}}{\rho h_1} \qquad (14)$$

In the interior, a Sverdrup balance exists and $\partial v_1/\partial t$ is negligible. The right side of (14) has negative sign since the geopotential gradient, although positive, is smaller in magnitude than the Ekman drift term. In the upwelling boundary layer $u_1 \to 0$ over the scale of the baroclinic radius to satisfy the kinematic boundary condition, but the right side of (14) changes relatively little, forcing $\partial v_1/\partial t < 0$. No slip at the coast and the viscous boundary layer (width 5 to 7 km for the present study) result in the development of a jet structure in the longshore flow. The existence of the jet is well documented (e.g., Mooers et al., 1975; Stevenson et al., 1974; Huyer et al., 1975) with equatorward speeds 0.20 to 0.30 m sec^{-1} in the jet maximum located 15 to 20 km offshore.

0.20 to 0.30 m sec^{-1} in the jet maximum located 15 to 20 km offshore.

Theory predicts an e-folding width of λ_I for the equatorward jet. The offshore side of the jet in Fig. 9c has an

e-folding width of 12 to 14 km, in good agreement with the observations of Huyer (1974). The e-folding width of the jet displays relatively little longshore variability.

Huyer (1974) compared geostrophic calculations from hydrographic observations to v-component time series from current meters off Newport. She concluded that ". . . the observed currents were mainly geostrophic during the period 5 to 20 July [1972] even though the winds were variable." Comparing Fig. 9c with Figs. 6b and 8b demostrates the geostrophic nature of the baroclinic jet. The stronger barotropic mode of Case III produces somewhat larger equatorward speeds than in the flat bottom case. Geostrophic calculations using the sea surface slope of Fig. 8b predict a v_1 of $\sim$ 0.22 m sec^{-1} for the region $y \simeq -230$, in excellent agreement with Fig. 9c.

Longshore variability is noticeable in both the flat bottom and topography cases, both exhibiting a decrease in the jet maximum with increasing latitude.

Similarity in the longshore flow between the flat and topography cases does not, in this case, imply a lack of influence of topography on the longshore flow. In the topography case, a weaker E-W baroclinic pressure gradient will cause a weaker baroclinic equatorward flow. However, this effect is somewhat masked in the topography case by the stronger barotropic mode. Comparison of Fig. 9c with the upwelling pattern of Fig. 6b shows how areas of stronger

equatorward flow coincide with favored areas of upwelling.

One aspect of the upper layer flow, although not depicted here, is noteworthy. Huyer (1974), in comparing currents at station DB-7 (x = 18, y = 70) to those on the line off Yaquina Head (y = 50), has observed that the longshore current seems to diverge as it moves onto the widening shelf. The model solutions also show a divergence in the upper layer streamline vectors in the same vicinity.

e. Lower layer flow

It is in the lower layer that we expect bottom topography to exert its greatest influence. Fig. 10 compares zonal flow in the lower layer of Case I to that for Case III. Obviously, the topography has a strong effect on the offshore and longshore structure of u_2. Overlaying Fig. 10b with the topography transparency aids the analysis. There are several main features of the onshore-offshore flow pattern. Each develops before day 1 and persists qualitatively, although affected by oscillations of an inertial time scale. Notice the region of strong onshore flow of ~ 0.03 m sec^{-1} just south of the cape. Although this feature of the flow appears to be associated with the coastline variation, the flat bottom case exhibits no such feature. In fact, flow south of the cape in Case I is directed offshore! In the topography case onshore flow is relatively strong, ~ 0.01 m sec^{-1}, nearshore for most of the N-S extent of the basin. There is a region of strong offshore flow with axis at y $\simeq$ 50.

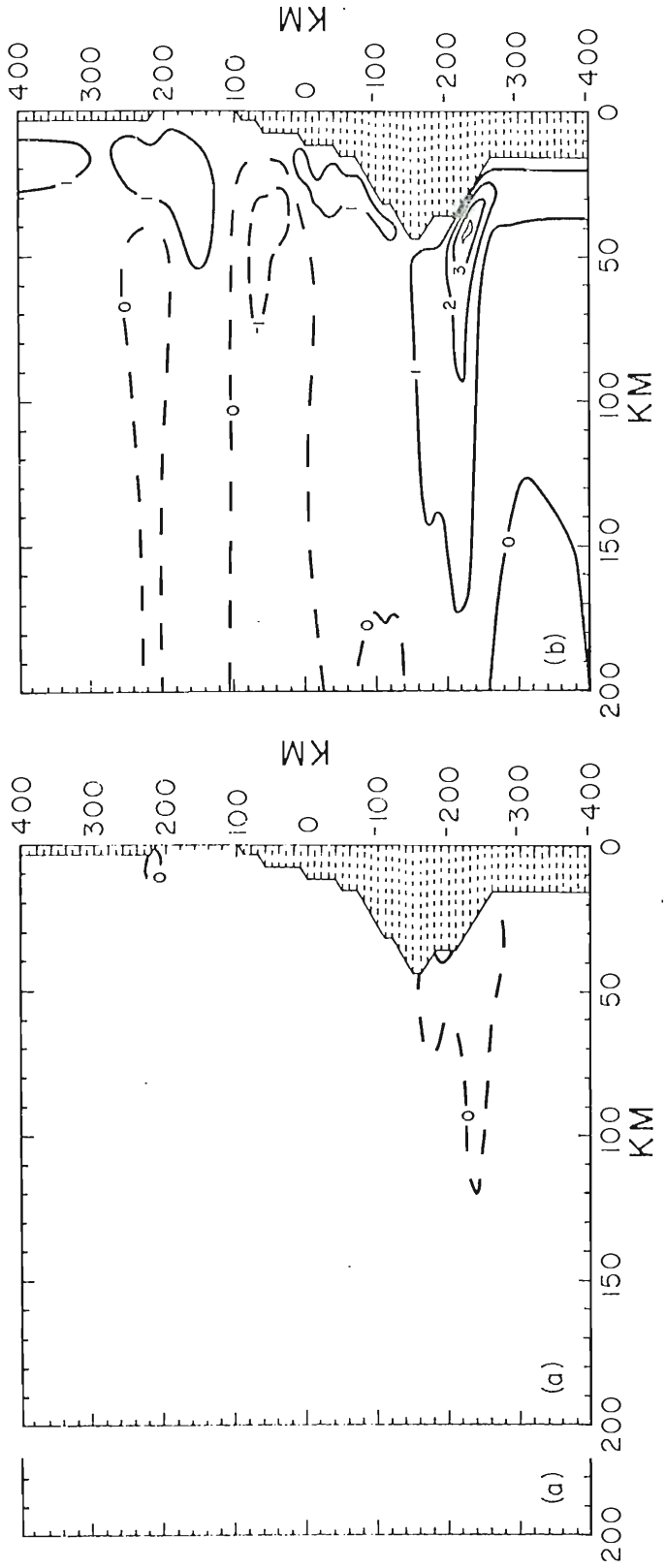

Fig. 10. Lower layer E-W velocity component (m sec^{-1} × 10^{-2}) at day 5 for Case I in (a) and Case III in (b). The same contour interval is used in both fioth figures.

Mean velocities from the CUE-I moored current meter array, as tabulated by Huyer (1974) for a period of generally southward winds, indicate mean zonal velocities for deep flows to be generally ≤ 0.01 m sec^{-1}. The deep current meters at NH-10 and NH-15 ($x \simeq 25$ to 30, $y \simeq 50$) show qualitative agreement with Fig. 10b, but the NH-20 deep flow is directed onshore, contradicting the model results.

Zonal flow in the lower layer can be understood in terms of the linear y-momentum equation (Hurlburt and Thompson, 1973)

$$\frac{\partial v_2}{\partial t} + f u_2 = - g \frac{\partial}{\partial y} (h_1 + h_2 + D) + g' \frac{\partial h_1}{\partial y} - \frac{\tau_{By}}{\rho_2 h_2} \qquad (15)$$

In the interior a geostrophic balance holds. The kinematic boundary condition forces u_2 to zero in the upwelling region and, for the flat bottom case, $\partial v_2/\partial t > 0$. For the case with E-W sloping topography, offshore transport over the shelf is approximately the same as in the interior. Thus, mass continuity requires the onshore flow over the shelf to become supergeostrophic, forcing $\partial v_2/\partial t < 0$ until a frictional balance is achieved in (15).

The generally stronger onshore flow nearshore noted above can thus be understood as a consequence of mass continuity and the rising topography. If the position of the

above can thus be understood as a consequence of mass continuity and the rising topography. If the position of the onshore maximum south of the cape in Fig. 10b is compared to that of the net x-transport in Fig. 12b (which closely

resembles the lower layer zonal transport), the following can be noted. The velocity maximum is inshore of the transport maximum, demonstrating how u_2 becomes supergeostrophic meeting the continuity constraint.

Fig. 10b demonstrates that topographic variations affect the pattern of onshore flow well beyond the region of sloping topography, producing barotropic flows which seem to be governed by the barotropic radius of deformation. In particular, the strong onshore flow just south of the cape appears to be due to a divergence in v_2 (see Fig. 11a). Comparing Figs. 10b and 6b shows a generally stronger onshore flow in areas of active upwelling.

Longshore variations in deep onshore flow have been observed (Shaffer, 1974) in the NW Africa upwelling region. For canyons of approximately half the width of those in the Oregon area, Shaffer observed neutrally buoyant floats to move shoreward along the canyon axis. He concluded: "The main 'onshore' compensation flow takes place along the axis of the canyon." This is not observed in Fig. 10b. Instead, a pattern of offshore transport north of a ridge, and onshore transport south of a ridge is seen, with the exception of the ridge at $y \simeq -150$. This pattern agrees with the results of Hurlburt (1974) for a simple symmetric ridge. The NW Africa observations and the area of onshore flow north of the ridge at $y \simeq -150$ in Fig. 10b lead us to speculate that the longshore distribution of deep zonal flow is quite sensitive to

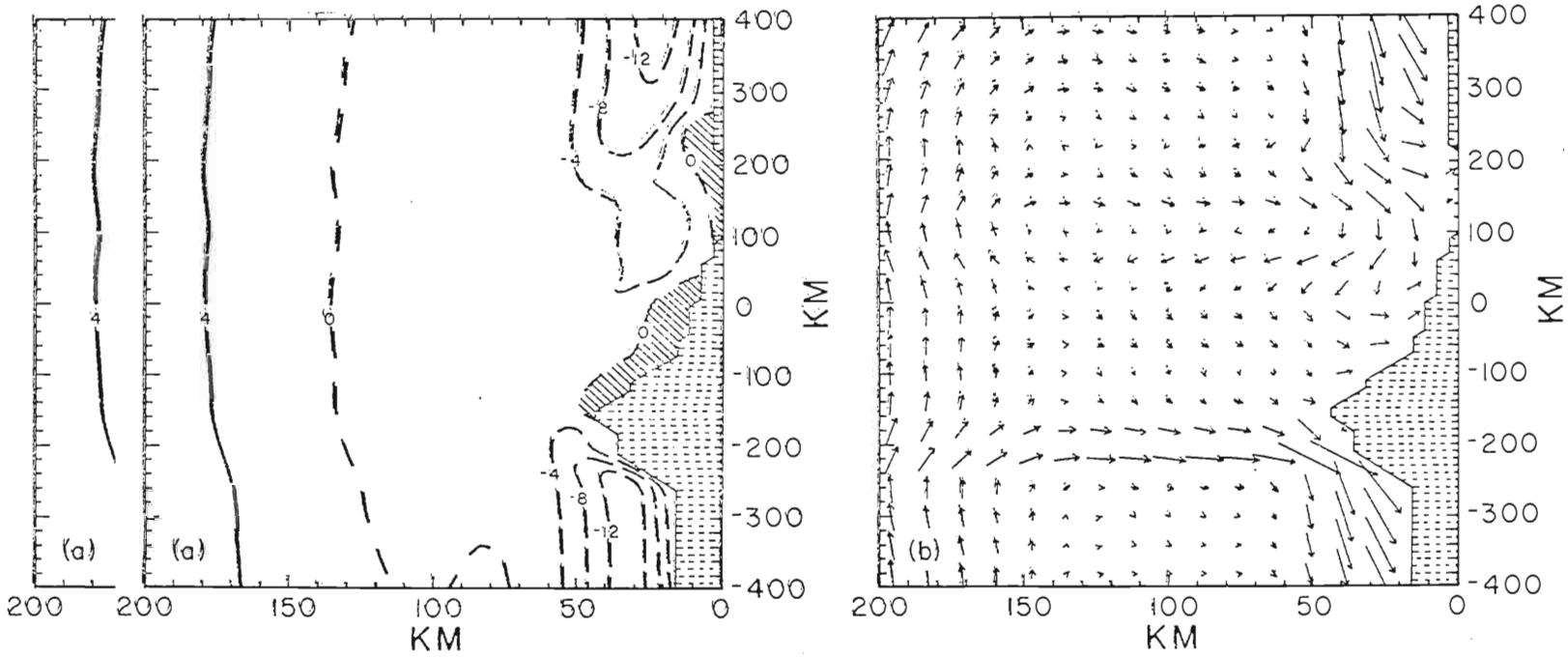

Fig. 11. Lower layer N-S component of velocity (m sec^{-1} × 10^{-2}) at day 5 for 5 for Case III in (a). Lower layer velocity vectors (b) for Case III at day 5. The arThe arrows define streamlines, not geographical direction in this and other vectorvector plots, i.e., the x component is multiplied by 800/200 = 4. The length of theof the arrows is scaled by the longest arrow in the frame.

the longshore scale of the topographic variation.

Fig. 11a presents contours of the lower layer N-S component of velocity for the topography case at day 5, and Fig. 11b the lower layer velocity streamline vectors for the same case. For the flat bottom case (not shown) meridional flow at day 5 is everywhere weakly poleward in the lower layer, with a jet structure developing in the upwelling zone similar to that seen by Hurlburt (1974) for a β-plane flat bottom, meridional coast case. But the picture in Fig. 11a is quite different. Topography induces distinct variations in both the offshore and longshore structure of the flow. In particular, the equatorward jet structure of the y-independent north and south boundary regions implies the dominance of a strong barotropic mode there. In the region of longshore varying topography, the barotropic mode is much reduced; in fact, two regions of poleward flow develop (shaded areas of Fig. 11a). The more southern region appears during the first day of integration developing first just north of the main cape. The other area of poleward flow develops first at y ≃ 210 at about day 1.25. Topography clearly has a significant effect on the longshore flow.

A poleward undercurrent, coincident with the upwelling season has been observed in Oregon (Mooers et al., 1975; Huyer, 1974). Huyer has observed statistically significant deep poleward flow at several CUE-I moored current meter
Huyer, 1974). Huyer has observed statistically significant deep poleward flow at several CUE-I moored current meter stations, no poleward flow at others. The CUE-I data do not

provide a detailed description of the offshore dependence of the deep flow; however, its strength is not observed to decrease with distance offshore. In the upwelling boundary layer the E-W barotropic and baroclinic pressure gradients compete in driving the geostrophic longshore flow. Huyer concluded that there is a persistent vertical shear in the longshore flow during the upwelling season which varies with location and time. The shear was observed to obey the thermal wind (geostrophic) relation.

Hurlburt and Thompson (1973) have reviewed theoretical explanations of the poleward undercurrent and explained how the β effect can produce a longshore pressure gradient sufficient to reduce the barotropic mode, allowing poleward flow to develop. The poleward undercurrent observed in the present study is similar to that which developed for sharp shelf cases in the x-z models of Hurlburt and Thompson (1973) and Thompson (1974), being restricted to the region immediately adjacent to the coast. As explained in the discussion of (15), u_2 becomes supergeostrophic over an E-W sloping bottom in response to requirements of continuity, forcing $\partial v_2/\partial t < 0$. Over the flat topography, a moderately increasing N-S pressure gradient in the lower layer coupled with a decrease in other terms of the y-momentum equation in the viscous boundary layer can allow the N-S pressure gradient to dominate very near the coast and $v_2 > 0$.
the viscous boundary layer can allow the N-S pressure gradient to dominate very near the coast and $v_2 > 0$.

In a linear time-dependent, continuously stratified f-plane model with E-W sloping, but y-independent topography,

Pedlosky (1974c) has found a poleward undercurrent to develop in response to bottom friction and the vorticity constraint imposed by the E-W sloping bottom. He observed that the undercurrent begins as a broad flow, but for times large compared to the barotropic spin-up time and small compared to the diffusive time scale, shrinks to a flow resembling that found by Hurlburt and Thompson (1973), nestled against the coast. Pedlosky concluded that this inshore counter-current gives way over diffusive time scales to a steady counter-current discussed in Pedlosky (1974b).

The feature of the undercurrent of most interest in the present study is its longshore variability. Comparison of Fig. 11a with the upwelling contours of Fig. 6b shows a tendency for areas of poleward (or weaker equatorward) flow to coincide with areas of stronger upwelling, i.e., an increased baroclinic mode.

Hurlburt (1974) has investigated the effects of N-S sloping topography on the development of the poleward undercurrent. Two cases, using wedge-shaped topography with N-S slopes of opposite sign showed the following. Topography sloping upward towards the north ($\beta_T > 0$) resulted in an enhanced poleward flow near the shore. The opposite was true for $\beta_T < 0$. As previously discussed, the topographic beta effect can act in (8) to affect the longshore pressure gradient - and thus affect the strength of the poleward undercurrent. To summarize, regions of $\beta_T > 0$ would be expected

to exhibit stronger poleward flow than regions for which $\beta_T < 0$. Hurlburt states that the fundamental scale of influence seems to be the barotropic radius of deformation.

Overlaying Fig. 11a with the bottom topography, we see general agreement with the predictions of the β_T effect. It should also be noted that the undercurrent is more likely to develop in areas where the shelf is wider. The equatorward barotropic mode is more effectively reduced by $\int \beta v_1 dx$ in these areas with wider shelves.

Several interesting features of the flow are apparent in Fig. 11b. A strong divergence occurs in the longshore flow near the cape with an associated response in the onshore flow dictated by continuity. There is a general tendency to follow the isobaths, but regions of cross-isobath flow do occur. Oregon observations (Huyer, 1974) indicate that the orientation of the major axis of flow is determined by the bathymetry, tending to be oriented along the local bottom contours. However, mean cross-isobath flow has been observed at all levels at the DB-7 current meter string (x = 18, y = 70), and the model results indicate cross-isobath flow there. An anticyclonic gyre (axis at y ≃ 100) with scale governed by the barotropic radius seems to be associated with the main canyon. A weaker gyre exists at x ≃ 130, y ≃ 240. Their positions remain quite stationary during spin-up.

canyon. A weaker gyre exists at x ≃ 130, y ≃ 240. Their positions remain quite stationary during spin-up.

f. Net transports

Net E-W transport for the flat case and topography case

at day 5 are compared in Fig. 12. Mass is fairly well conserved in planes perpendicular to the coast for the flat case - but the case with bottom topography displays a drastic departure from mass balance in the x-z plane. Two-dimensional (x-z) models of the Oregon coast conserve mass in an E-W plane, but the observations do not agree. The x-y model shows why. Fig. 12 conclusively shows that for the Oregon region, a three-dimensional representation of the current field is essential to explain the observed features.

The effects of topography are clearly seen in the picture of zonal barotropic flow (Fig. 12). The following pattern is <u>always</u> seen in Fig. 12b: offshore net transport north of a ridge and onshore net transport south of a ridge. The observed pattern agrees with the results of Hurlburt (1974) who concluded that the dominant scale of influence in the longshore variation of barotropic transport was the ridge width. Variations in the barotropic transport perpendicular to the coast are in response to fluctuations in the longshore flow caused by the topographic β effect.

Fig. 13a shows N-S mass transport in the lower layer for the topography case at day 2.5. The corresponding net N-S transport is shown in Fig. 13b. Overlaying Fig. 13b with the topography transparency reveals several features of the net flow. Strong equatorward transport is seen over

the net flow. Strong equatorward transport is seen over

areas of sharper E-W slope in regions where the isobaths parallel the meridians. Note how Hecata Bank "pushes" the

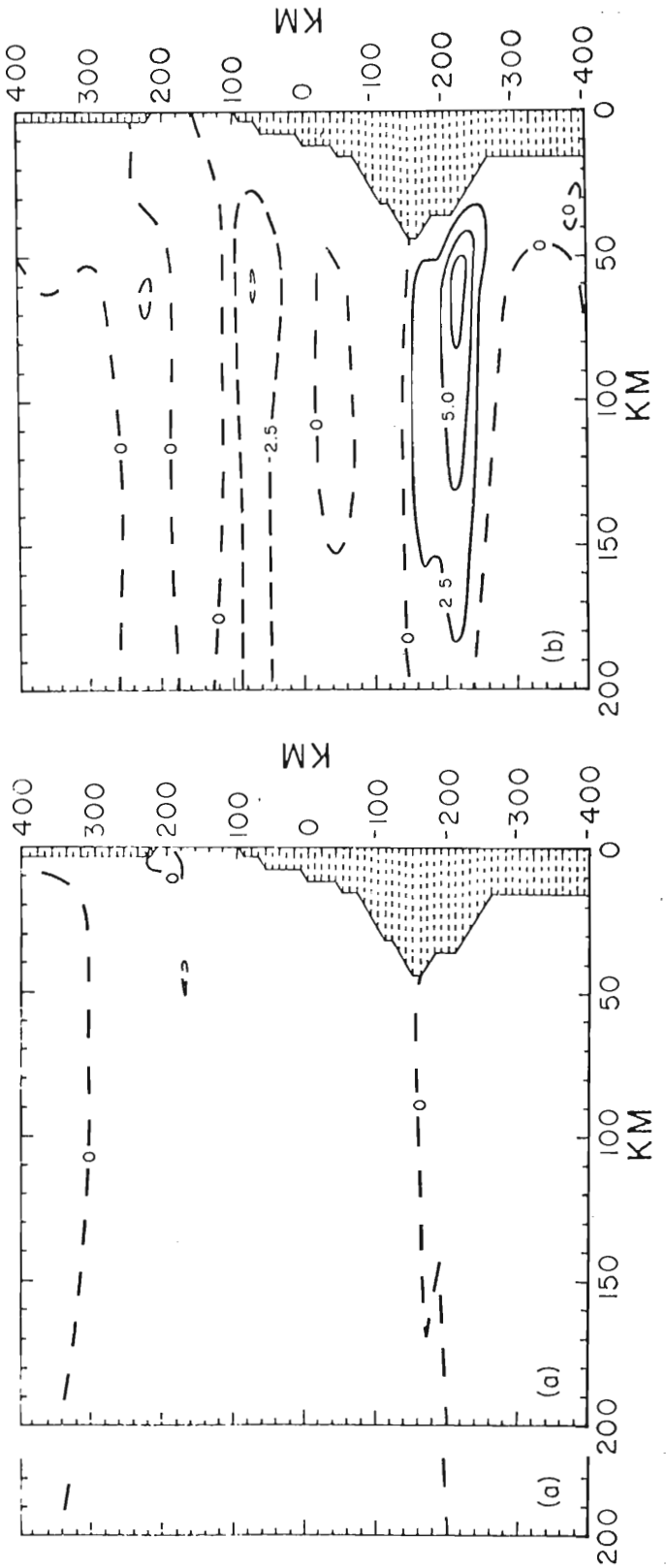

Fig. 12. Vertically-integrated E-W component of mass transport (kg m^{-1} sec^{-1} x 10^3) at day 5 for Case I in (a) and Case III in (b). The same contour intervalterval is used in both figures.

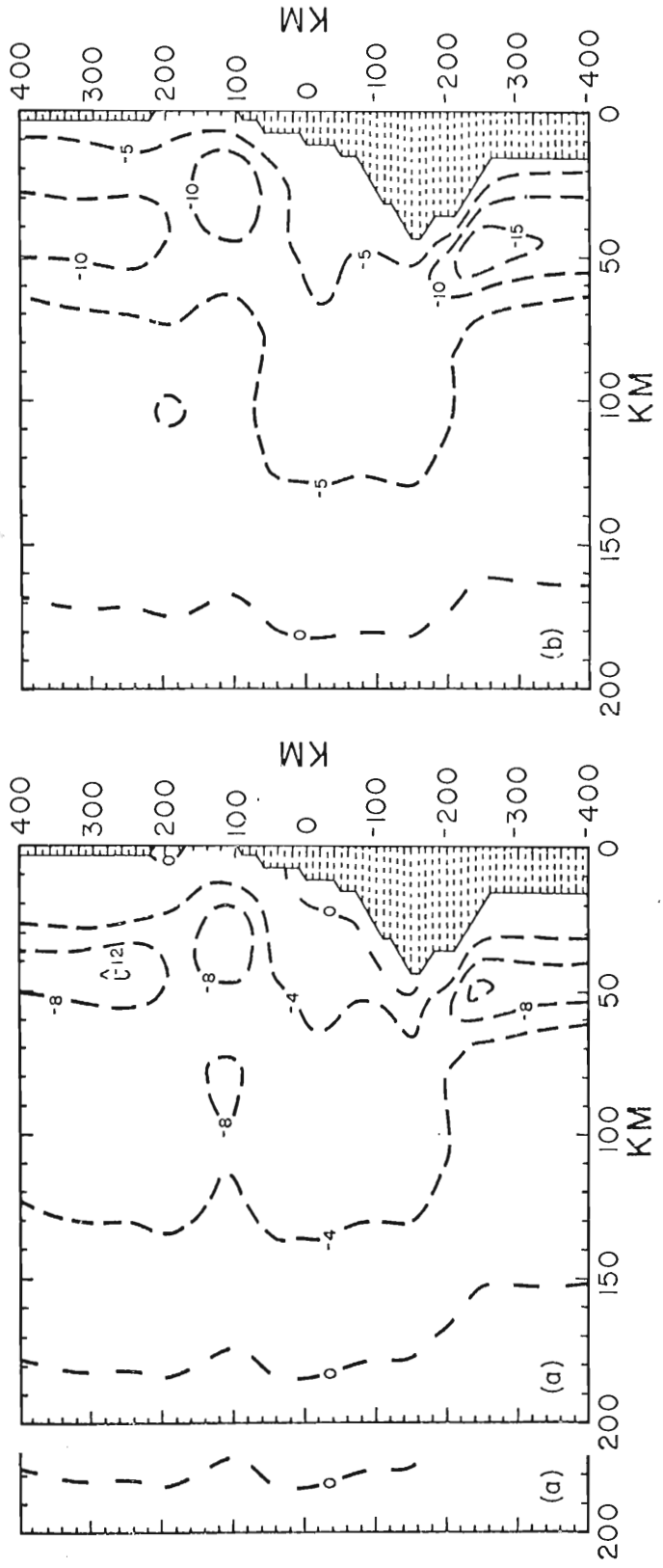

Fig. 13. N-S component of lower layer mass transport (a) for Case II at day 2.5 and the vertically-integrated N-S component of mass transport (b) at day 2.5 for Case II. All contours are labeled in kg m^{-1} sec^{-1} x 10^3. Note that different contour intervals are used in (a) and (b).

transport contour offshore. Comparison with Fig. 13a shows that at day 2.5 variations in the net N-S transport mirror those of the lower layer. Fig. 14a shows the net N-S transport for the topography case at day 5. Net transport vectors are shown in Fig. 14b. Note the strong similarity to the lower layer vectors of Fig. 11b. The intense barotropic onshore transport just south of the cape is clearly seen to be a consequence of a divergence in the net N-S flow. Comparison of the baroclinic N-S transports for the flat and topography cases show significant differences, indicating that for longshore flow topography influences both the barotropic and baroclinic modes. A time series of barotropic vectors shows that streamlines generally follow the bottom contours within the 70 km nearest the coast independent of time during spin-up. Features of the flow further offshore, however, develop with time. Notice that the center of the gyre (axis at y = 100) corresponds to the closed contour of free surface anomaly in Fig. 8b.

As mentioned earlier in this section, strong topographic Rossby waves can be excited by variations in bottom height in the term $\text{curl}_z\,[(\tau_s - \tau_B)/h]$ of Eq. (12). Such Rossby waves are evidenced by the poleward flow in Fig. 14. These topographic Rossby waves were excited independent of the initial state. In this β-plane model, the topographic Rossby waves and consequent westward intensification appear primarily responsible for the return flow of the topographi-

Rossby waves and consequent westward intensification appear primarily responsible for the return flow of the topographi-cally induced barotropic coastal current in the eastern ocean (Hurlburt, personal communication).

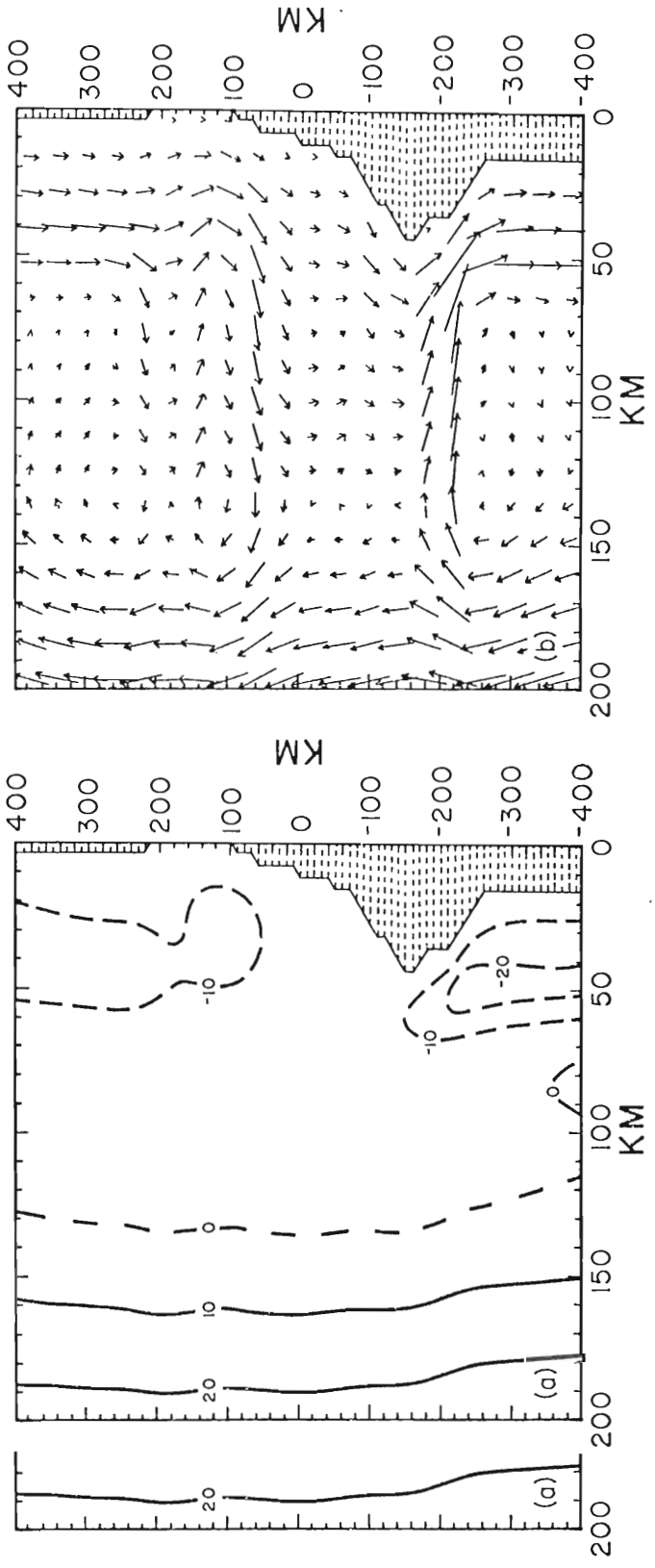

Fig. 14. Mass transport for Case III at day 5. In (a) contours of total barotrcarotropic N-S transport (kg m^{-1} sec^{-1} x 10^3), and in (b), the barotropic transport veort vectors.

6. SPIN-DOWN

To investigate the relaxation phase of upwelling, the winds have been varied in the simplest manner possible. In Cases I and II, the wind stress of Fig. 5 has been shut off at day 2.5 and the integration continued to day 5. The emphasis of our analysis will be on the pattern of decay of the longshore current and the upwelling, using comparisons of the picture at day 2.5 to that at subsequent times.

a. Zonal flow

Upper layer E-W flow during spin-down is strongly dominated by inertial oscillations. Two features observed during spin-up persist during relaxation: (1) a small pocket of offshore flow just north of the cape, and (2) an area of onshore flow south of the cape. Persistence during spin-down of onshore flow in this area suggests a testable hypothesis: the existence of an onshore jet during the upwelling season just south of Cape Blanco. Greater upper layer onshore transport in areas where the pycnocline is relaxing faster would be expected, and the model is in qualitative agreement.

In the lower layer at day 5, both the flat bottom and topography cases are characterized by weak u_2 flow, ~ 0.01 m

In the lower layer at day 5, both the flat bottom and topography cases are characterized by weak u_2 flow, ~ 0.01 m

sec^{-1} compared to ~ 0.03 m sec^{-1} at day 2.5. The pattern

of longshore variability has reversed (N-S lower layer flow has also reversed, now being generally poleward). The general rule is now: onshore flow north of ridges, and offshore flow south of ridges. One area of onshore transport corresponds to the area of strongest upwelling in Fig. 18b.

b. Meridional flow

The meridional component of upper layer flow for Case I, days 2.5 and 4.25, is shown in Fig. 15. By day 4.25 the equatorward jet has decayed, most quickly in the northern part of the basin. By comparison, in the flat bottom case (not shown), the upper layer flow at day 4.25 is equatorward everywhere and the jet has decayed uniformly longshore. A time series of v_1 shows that the area of stronger southward flow associated with the head of the main canyon diminishes and moves northward after the wind is shut off. The reasons for this northward movement will be discussed in Section 6c. Of particular interest are two areas of upper layer poleward flow nearshore in Fig. 15b. Huyer (1974) has reported shallow poleward flow at the NH-3 site (x = 10, y = 45), which coincided with a barotropic reversal in the currents. Although the E-W sea surface slope in the upwelling zone is still negative at day 4.25, the areas of poleward flow in Fig. 15b coincide with two areas of relatively small E-W slope. We believe inertial oscillations are the dominant mechanism acting here, for at day 5 (see Fig. 16c) one of the regions is again showing equatorward, but relatively weak equatorward, flow.

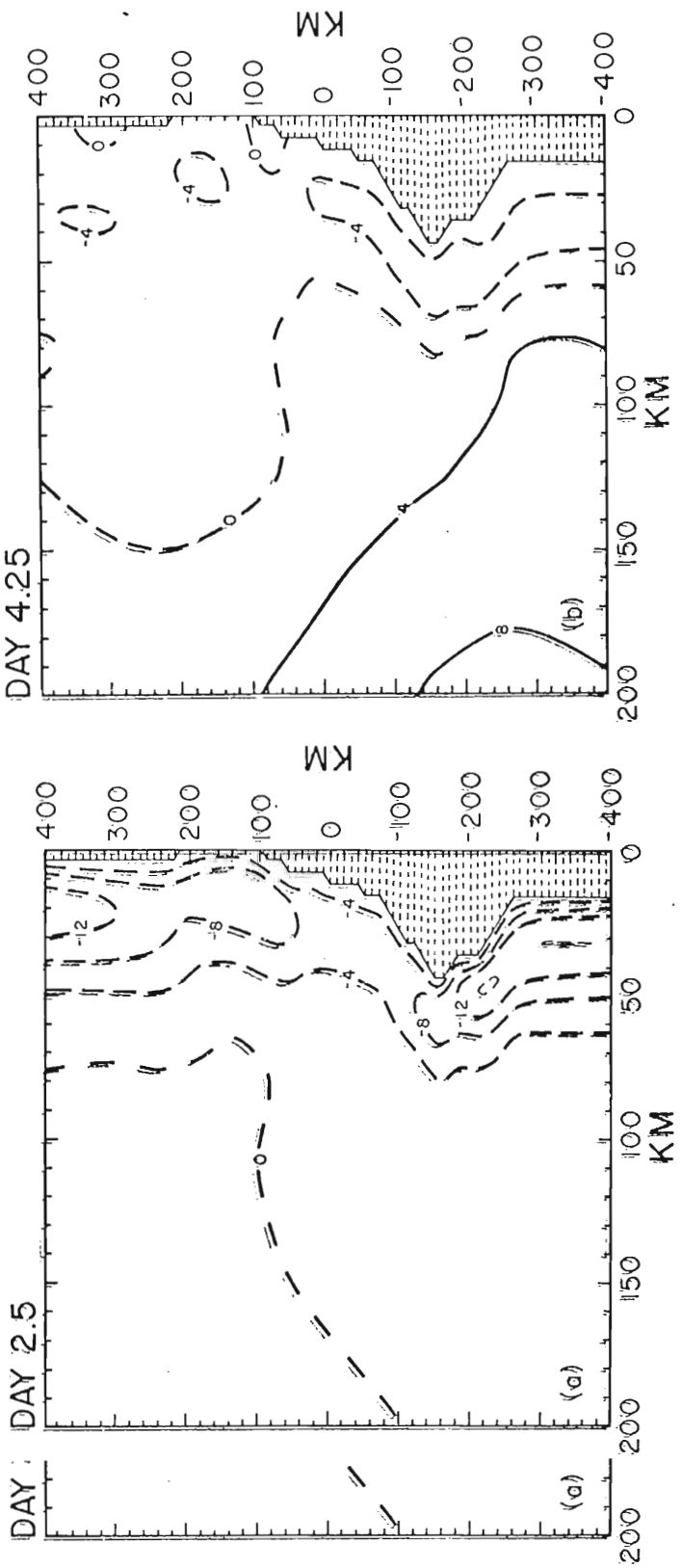

Fig. 15. N-S component of upper layer velocity in m sec^{-1} $\times 10^{-2}$ for Case IIase II at day 2.5 in (a), and at day 4.25 in (b). The wind was shut off at day 2.5ay 2.5.

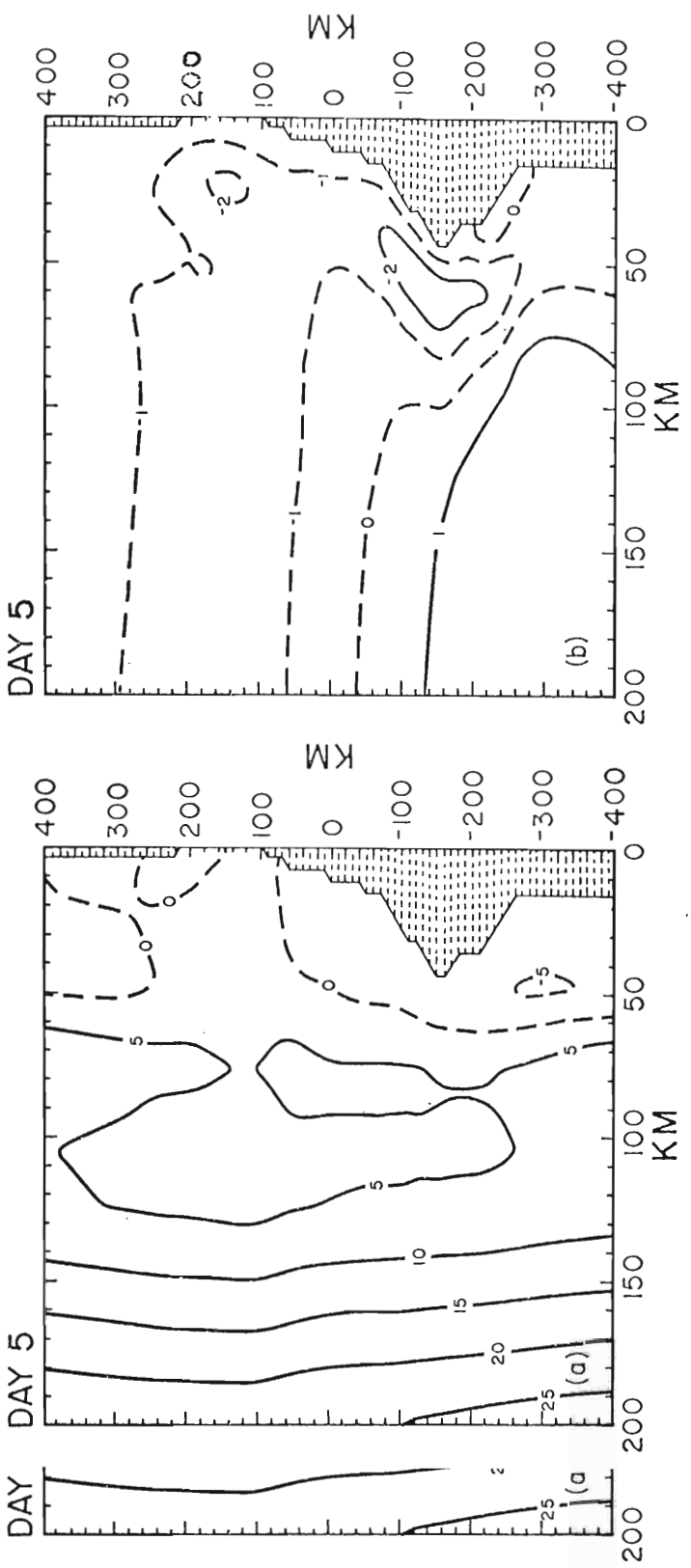
DAY
DAY 5
KM
400
300
200
100
0
-100
-200
-300
-400
0
50
100
150
200
25
20
15
10
5
0
-5
(a)
(b)

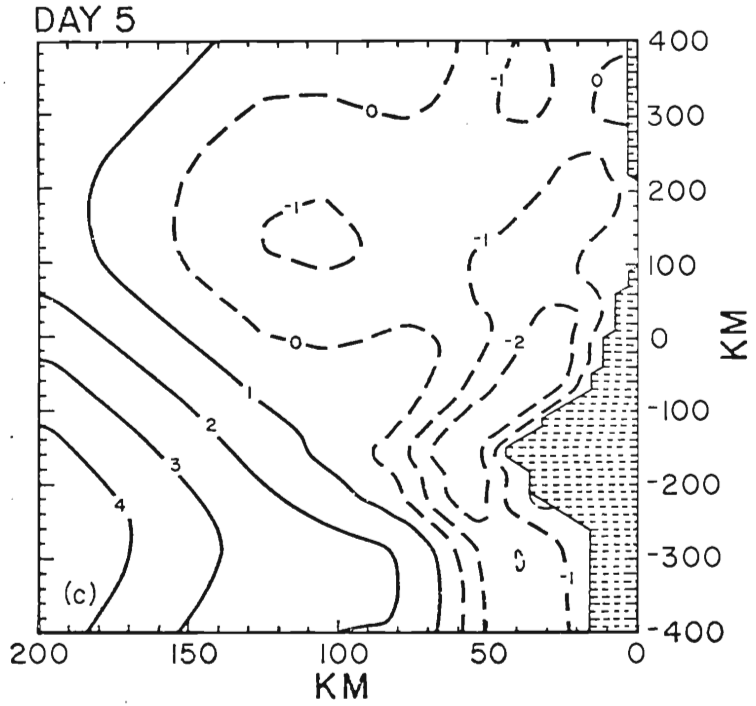

Fig. 16. Longshore (N-S) mass transport (kg m^{-1} sec^{-1} × 10^3) for Case II at day t day 5. In (a), the vertically-integrated N-S transport, in (b) the baroclinic N-S tra-S transport with sign appropriate for the upper layer and in (c) the upper layer N-S mas-S mass transport. Note the contour interval used in (a) is different from that used insed in (b) and (c). The wind was shut off at day 2.5.

Fig. 16 shows how the upper layer N-S transport is composed of barotropic and baroclinic modes. Although there is some minor longshore variation in the barotropic mode, most of the longshore structure in the upper layer meridional flow is seen to be due to the baroclinic mode. The pattern of N-S flow in Fig. 16b is clearly explained by the baroclinic E-W pressure gradient, as shown in Fig. 18b (contours in Fig. 16b are labeled with signs appropriate for the upper layer). Notice that the baroclinic mode is poleward nearshore in the region y = -200 to y = -280 in Fig. 16b.

Development of lower layer poleward flow during spin-down is portrayed in Fig. 17. At day 2.5 a barotropic southward jet exists in the northern and southern regions, with two areas of poleward flow near the coast. During spin-down, these two areas develop until, from day 3.75 on, there is poleward flow nearshore everywhere from the cape northward. This agrees with observations (Mooers and Allen, 1973) which indicate the poleward undercurrent over the shelf occurs more frequently after upwelling events relax. A time series of v_2 shows that the equatorward jet in the northern boundary region, with axis at x = 20 at day 2.5, shifts offshore as it weakens. At day 5 its axis is at x = 40. During this time a poleward jet has developed inshore of the equatorward jet.

The longshore variability of the poleward undercurrent

a poleward jet has developed inshore of the equatorward jet.

The longshore variability of the poleward undercurrent is interesting. During spin-up it is found only in certain areas favored by topography. A y-t plot of free surface

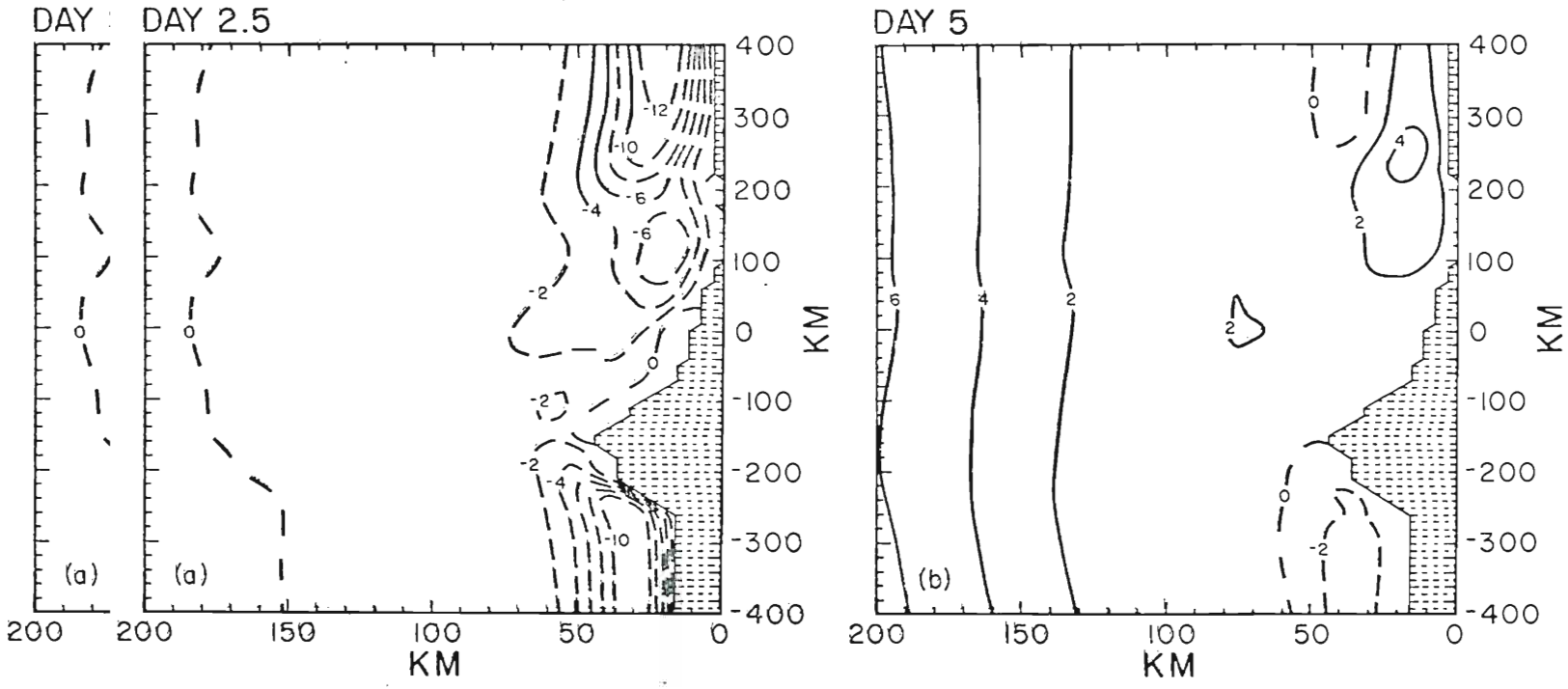

Fig. 17. N-S component of lower layer velocity in m $sec^{-1} \times 10^{-2}$ for Case II at day t day 2.5 in (a), and at day 5 in (b). The wind was shut off at day 2.5.

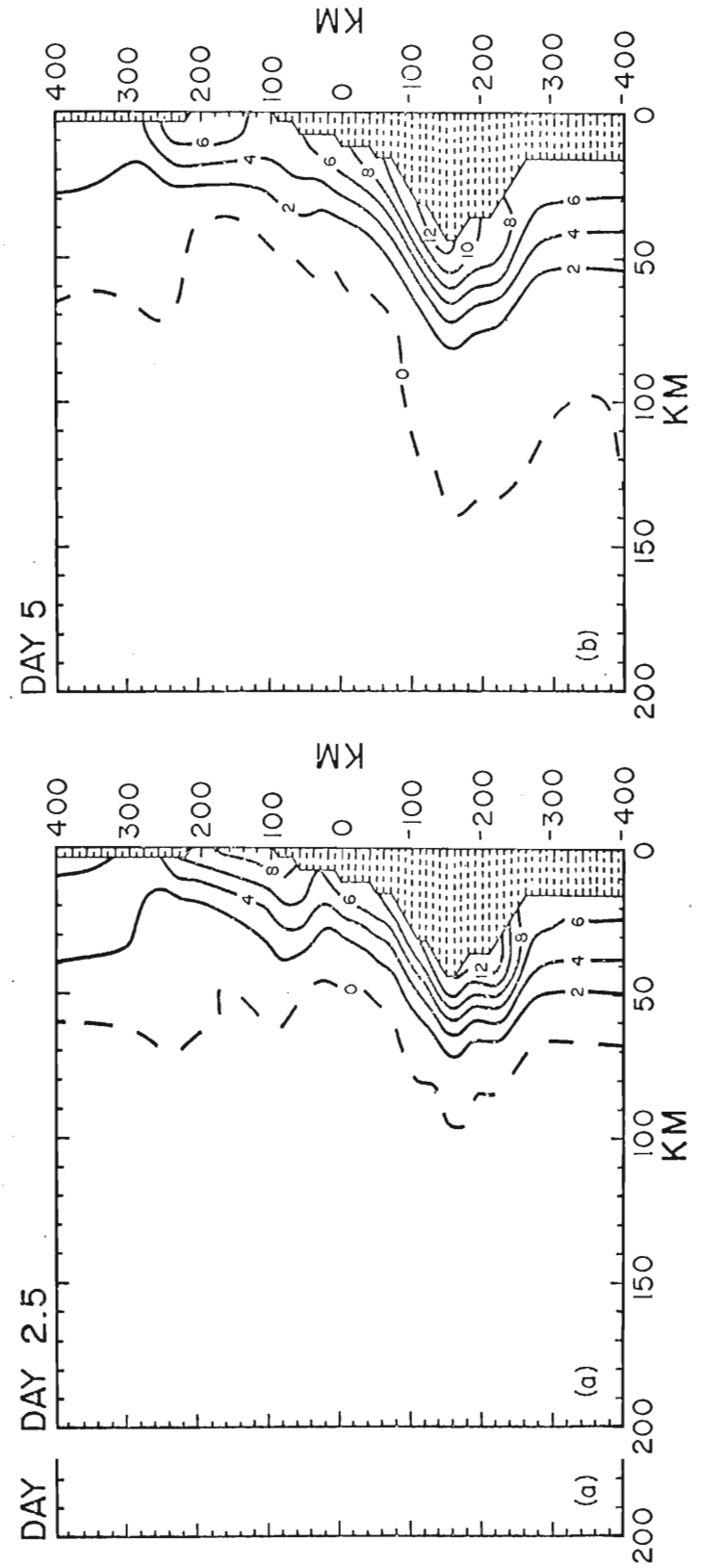

Fig. 18. Pycnocline height anomaly in m for Case II at day 2.5 in (a) and daynd day 5 in (b). The wind was shut off at day 2.5.

height at the coast (not shown) reveals that the barotropic mode begins to relax immediately when the wind is shut off at day 2.5. This, plus slower relaxation of the baroclinic mode produces the deep poleward flow. As explained by Hurlburt and Thompson (1973), as $u_1 h_1 \rightarrow 0$ during spin down, $u_2 h_2 \rightarrow 0$ also over an inertial period. Then, from Eq. (15), $\partial v_2/\partial t > 0$ since the N-S pressure gradient decays more slowly.

Persistent equatorward flow south of the cape can be explained by comparison of Figs. 16a and 11a. Since the undercurrent is a baroclinic flow, a sufficiently strong barotropic mode can mask the poleward current. Fig. 11a shows that the area south of the cape is such an area. This interesting contrast in the flow direction north and south of the cape leads us to predict the following. If two current meters were moored at the 100 m depth during upwelling season, one north and one south of Cape Blaco, the southern current meter would show a mean flow equatorward relative to that north of the cape.

c. Upwelling

The behavior of coastal upwelling during spin-down is represented in Figs. 18 and 19. In Fig. 18, the pattern of pycnocline displacement at day 2.5 is compared to that at day 5 for the topography case. Figs. 19a and 19b present (for Cases I and II, respectively) y-t plots of pycnocline height anomaly at the coast for the entire 5 day spin-up, spin-down cycle. Fig. 18 shows that the upwelling relaxes

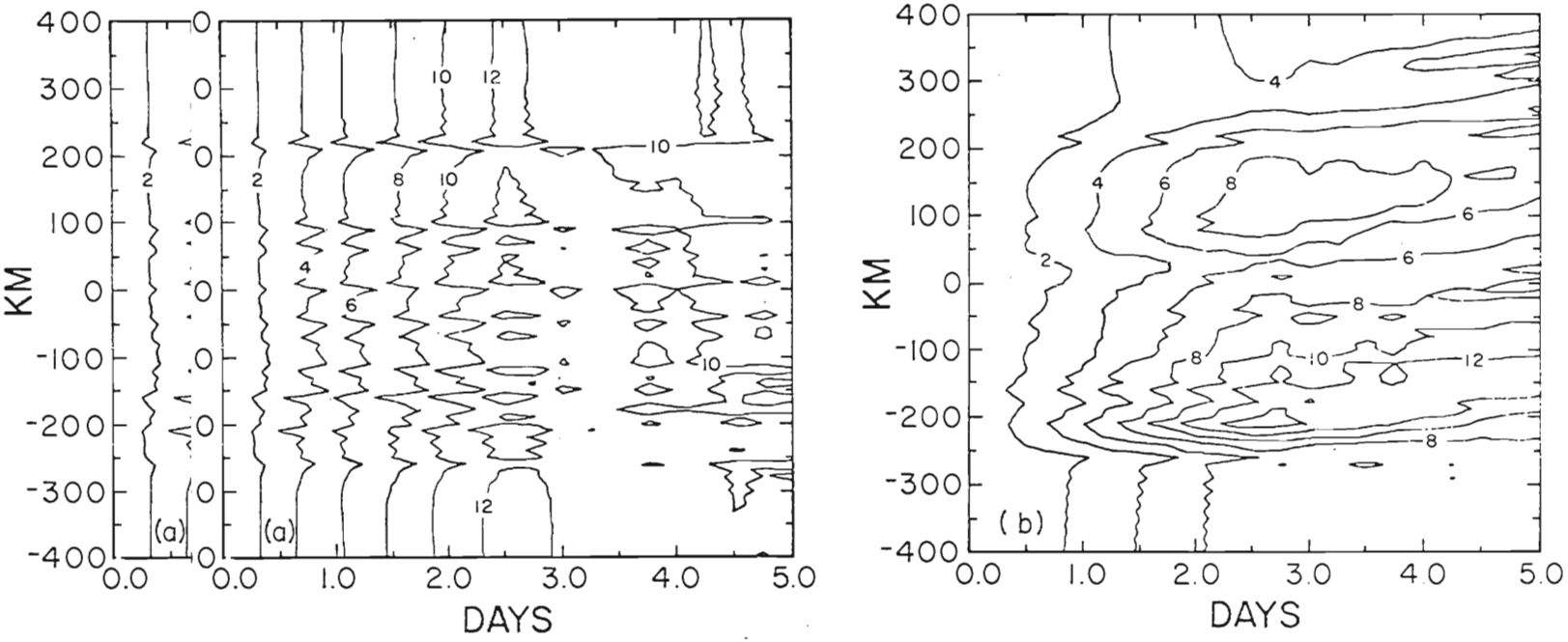

Fig. 19. Contours of pycnocline height anomaly at the coast in m as a functiounction of time and N-S position for Case I in (a) and Case II in (b). The wind was shuas shut off at day 2.5.

slightly during spin-down, but as noted by Huyer (1974): ". . . the effects of upwelling are easier to create than to destroy. . . . [they] do not disappear during several day periods when the wind is unfavorable to upwelling."

Longshore variations in the pattern of decay are relatively slight for the flat bottom case (see Fig. 19a). Upwelling seems to "hang on" longer south of the cape. Hurlburt (1974) observed in numerical model results that coastline variations can excite large amplitude internal Kelvin waves. No such waves are noticeable in the flat bottom case.

Northward propagation of the upwelling disturbance is quite apparent in the case with topography. Notice that the area of 12 m + upwelling south of the cape in Fig. 18a propagates northward, and at day 5 is located just north of the cape (Fig. 18b). Also, the area of relatively strong nearshore upwelling at the head of the main canyon in Fig. 18a has propagated northward explaining the northward movement of the region of relatively strong equatorward flow in Fig. 15. Poleward propagation of the upwelling appears in Fig. 19b as positive slope in the y-t contours. This poleward propagation of the disturbance is interpreted as a baroclinic continental shef wave.

Gill and Clarke (1974), in discussing shelf waves in baroclinic continental shef wave.

Gill and Clarke (1974), in discussing shelf waves in terms of an analytical model, stated: " . . . the upwelling

problem is also the shelf wave problem." For cases including both stratification and shelf-like bottom topography, they find the free modes have features of both shelf waves and internal Kelvin waves. Allen (1975), in an analytic two-layer model with y-independent shelf-slope topography, has investigated the nature of coupling between the barotropic and baroclinic modes for coastal trapped waves caused by bottom topography. He found that internal Kelvin waves can force a barotropic motion which extends out over the continental slope.

An estimate of the phase speed for the wave observed in Figs. 18 and 19b can be had by noting that the northern terminus of the 12 m isoline moves approximately 50 km in the 2.5 day spin-down period giving a phase speed of 0.25 m sec^{-1}. Slopes of the y-t contours in Fig. 19b yield the same estimate. By comparison, the speed of an internal gravity wave (at the coast) is given by

$$\sqrt{\frac{g' h_1 h_2}{h_1 + h_2}} .$$

For h_1 = 10 m, the internal wave phase speed is $\sim$ 0.40 m sec^{-1}. Observations of baroclinic waves for Oregon are sparse, although barotropic continental shelf waves have been observed (e.g., Mooers and Smith, 1968; Cutchin and Smith, 1973).

been observed (e.g., Mooers and Smith, 1968; Cutchin and Smith, 1973).

An interesting feature of the solutions (visible in both Figs. 6b and 19b) is the apparent longshore variability

in shelf wave propagation during spin-up. Although no northward propagation of the upwelling is noticeable during spin-up south of $y \simeq 0$, the pattern of upwelling near the canyon is obviously propagating northward even under forced conditions, at a speed of ~ 0.25 m sec^{-1}. When the winds are shut off, northward propagation is observed along the entire N-S extent of the basin.

7. CRITIQUE

Certainly, our efforts in modeling the onset of coastal upwelling suggest several ways in which significant improvements can be made. Inclusion of a more realistic wind stress, with time dependency in a three-dimensional model is left for further work. The importance of the omission of thermodynamics has been discussed. A careful treatment of the problem of initialization is called for.

Even using the complex topography of Fig. 4b, our model of Oregon upwelling is an idealization of the actual underwater topography, as a glance at Fig. 4a will indicate. Although the principal scales of variation have been preserved, bottom slopes are too gradual in comparison to actual Oregon topography, and no realistic shelf break is included. Finer resolution must be used in x and y to include the shelf break and steep bottom slopes, requiring a larger usage of computer core storage and a smaller time step. These economic considerations begin to weigh heavily in an assessment of the two-layer model's applicability to the problem under study here. For instance, a case typical of those discussed in Sections 5 and 6, with $\sim$ 3200 grid points, used roughly 25 minutes of CDC 6600 CPU time per day of model run. However in Sections 5 and 6, with $\sim$ 3200 grid points, used roughly 25 minutes of CDC 6600 CPU time per day of model run. However use of the y-stretching option (not exploited in this study)

should result in substantial savings of core storage. Also, a more efficient version of the model, which makes use of less expensive extended computer core storage, now exists (Hurlburt, personal communication). These features, plus careful case selection will, we believe, allow the two-layer model to continue to be not only an effective but an economic tool for understanding upwelling.

8. SUMMARY

The non-linear numerical model developed by Hurlburt (1974) has been used to investigate the effects of Oregon-like bottom topography on the onset and decay of the coastal upwelling circulation. The model is a wind-driven x-y-t, two-layer, β-plane model which neglects thermodynamics. The actual nearshore Oregon bathymetry was digitized and a Fourier analysis done to determine the dominant longshore scales of variation. A smoothed version of the topography was used. Cases were run with physical parameters typical of the Oregon region, the model being forced by a simple y-independent, time-independent wind stress. Economic considerations for three-dimensional numerical models of upwelling have been discussed.

Cases with varying initial states, topographies and wind stresses were compared using synoptic contour and vector plots of model solutions. Variations in bottom topography are found to play a very important role in explaining observed mesoscale features of the Oregon upwelling circulation. The region near Cape Kiwanda (y = 110 in Fig. 3) is shown to be an area of favored upwelling due to presence of an underwater mesoscale canyon. In general, for an equator-

shown to be an area of favored upwelling due to presence of an underwater mesoscale canyon. In general, for an equatorward wind stress, the pattern of longshore variation in

upwelling intensity is explained by the rule: greater upwelling equatorward of (and lesser upwelling poleward of) a canyon axis, consistent with the topographic β effect. Topographic variations are found to dominate over coastline irregularities in determining the longshore structure of upwelling. Specifically, our study indicates that the stronger upwelling observed near Cape Blanco is mainly due to local bottom topography rather than the cape itself.

Topography is seen to exert little influence on the pattern of upper layer offshore transport, but does influence the longshore structure of upper layer meridional flow by affecting the baroclinic mode. A great degree of variability in the N-S lower layer flow, including two regions with a nearshore poleward undercurrent, is explained by variations in the longshore pressure gradient induced by the topographic β effect. Irregularities in the barotropic onshore-offshore flow, on scales exceeding that of the sloping topography, respond to the topography induced variations in the longshore flow. Zonal mass balance is <u>not</u> seen for the Oregon upwelling regime, with net zonal transports always seen to follow the pattern: offshore transport north of a ridge and onshore transport south of a ridge under forcing by southward blowing wind.

Topographic Rossby waves are seen in the model solutions and their importance in the return flow of the topographically

Topographic Rossby waves are seen in the model solutions and their importance in the return flow of the topographically induced barotropic eastern ocean is discussed. The existence

of a relative onshore jet just south of Cape Blanco and relative northward deep flow north of Cape Blanco is predicted. During spin-down (and for some regions during spin-up) baroclinic continental shelf waves are observed in the pattern of the pycnocline height anomaly.

We conclude that the inclusion of realistic bottom topography is essential to an understanding of local upwelling and the longshore current structure of the Oregon region.

APPENDIX

LIST OF SYMBOLS

A	horizonatal eddy viscosity
C_I, C_B	drag coefficients for interfacial and bottom friction
$D(x,y)$	height of the bottom topography above a reference level
f	Coriolis parameter
f_0	Coriolis parameter at $y = 0$
g	acceleration due to gravity
g'	reduced gravity, $g(\rho_2 - \rho_1)/\rho_2$
h	total depth
h_1, h_2	instantaneous local thickness of the layers
H_1, H_2	initial thickness of the layers
L_ν	width of the viscous boundary layer in the y-momentum equation
L_s	width of the continental shelf
L_x, L_y	total extent of the model region in the x and y directions
t	time
u, v	barotropic components of velocity in the x and y directions
u_1, u_2	x-directed components of current velocity
v_1, v_2	y-directed components of current velocity
x, y, z	tangent plane Cartesian coordinates: x positive
v_1, v_2	y-directed components of current velocity
x, y, z	tangent plane Cartesian coordinates: x positive eastward, y positive northward, z positive upward.

β	df/dy
β_T	value of β simulated by N-S sloping topography
Δt	time increment in the numerical integration
Δx, Δy	horizontal grid increments in the x and y directions
λ_I	baroclinic radius of deformation
λ_E	barotropic radius of deformation
ρ, ρ_1, ρ_2	densities of sea water
σ_t	$(\rho_{s,t,0} - 1) \times 10^3$, where $\rho_{s,t,0}$ is the sea water density corrected to atmospheric pressure
τ_{sx}, τ_{Ix}, τ_{Bx}	x-directed tangential stresses at the surface, interface, and bottom
τ_{sy}, τ_{Iy}, τ_{By}	y-directed tangential stresses at the surface, interface, and bottom

REFERENCES

Allen, J. S., 1975: Coastal trapped waves in a stratified ocean (submitted to J. Phys. Oceanogr.).

Arthur, R. S., 1965: On the calculation of vertical motion in eastern boundary currents from determinations of horizontal motion. J. Geophys. Res., 70, 2799-2803.

Brunson, B. A., and W. P. Elliot, 1974: Steric contribution to the seasonal oscillation of sea level off Oregon. J. Phys. Oceanogr., 4, 304-309.

Crank, J., and P. Nicholson, 1947: A practical method for numerical evaluation of solutions of partial differential equations of heat-conduction type. Proc. Camb. Philos. Soc., 43, 50-67.

Cutchin, D. L., and R. L. Smith, 1973: Continental shelf waves: low-frequency variations in sea level and currents over the Oregon continental shelf. J. Phys. Oceanogr., 3, 73-82.

Elliot, D. L., and J. J. O'Brien, 1975: The mesoscale wind field over an upwelling region (to appear in Mon. Wea. Rev.).

Garvine, R. W., 1974: Ocean interiors and coastal upwelling models. J. Phys. Oceanogr., 4, 121-125.

Gill, A. E., and A. J. Clarke, 1974: Wind-induced upwelling, coastal currents and sea-level changes. Deep-Sea Res., 21, 325-345.

Grammeltvedt, A., 1969: A survey of finite-difference schemes for the primitive equations for a barotropic fluid. Mon. Wea. Rev., 97, 384-404.

Halpern, D., 1973: Variations in the density field during coastal upwelling. Tethys, (in press).

Halpern, D., 1974: CUE II wind stress at Station B. CUEA Newsletter, 3, No. 1, 18-22.

Halpern, D., 1974: CUE II wind stress at Station B. CUEA Newsletter, 3, No. 1, 18-22.

Holladay, C. G., and J. J. O'Brien, 1975: Mesoscale variability of sea surface temperatures (to appear in J. Phys. Oceanogr.).

Hurlburt, H. E., 1974: The influence of coastline geometry and bottom topography on the eastern ocean circulation. Ph.D. Thesis, Florida State University, 103 pp.

Hurlburt, H. E., and J. D. Thompson, 1973: Coastal upwelling on a β-plane. J. Phys. Oceanogr., 3, 16-32.

Huyer, A., 1974: Observations of the coastal upwelling region off Oregon during 1972. Ph.D. Thesis, Oregon State University, 149 pp.

Huyer, A., R. D. Pillsbury, and R. L. Smith, 1975: Seasonal variation of the alongshore velocity field over the continental shelf off Oregon. Limnol. Oceanogr., 20, 90-95.

Meneely, J. M., and E. S. Merritt, 1973: The potential of meteorological satellite cloud observations for delineation of significant features of coastal upwelling off Oregon. Final Report, Earth Satellite Corporation.

Mooers, C. N. K., and J. S. Allen, 1973: Final Report of the Coastal Upwelling Ecosystems Analysis Summer 1973 Theoretical Workshop. School of Oceanography, Oregon State University, Corvallis.

Mooers, C. N. K., C. A. Collins, and R. L. Smith, 1975: The dynamic structure of the frontal zone in the coastal upwelling region off Oregon (submitted to J. Phys. Oceanogr.).

Mooers, C. N. K., and R. L. Smith, 1968: Continental shelf waves off Oregon. J. Geophys. Res., 73, 549-557.

O'Brien, J. J., 1975: Models of coastal upwelling (to appear in Proceedings of NAS Symposium on Numerical Models of Ocean Circulation).

O'Brien, J. J., and H. E. Hurlburt, 1972: A numerical model of coastal upwelling. J. Phys. Oceanogr., 2, 14-26.

Pedlosky, J., 1974a: On coastal jets and upwelling in bounded basins. J. Phys. Oceanogr., 4, 3-18.

Pedlosky, J., 1974b: Longshore currents, upwelling and bottom topography. J. Phys. Oceanogr., 4, 214-226.

Pedlosky, J., 1974b: Longshore currents, upwelling and bottom topography. J. Phys. Oceanogr., 4, 214-226.

Pedlosky, J., 1974c: Longshore currents and the onset of upwelling over bottom slope. J. Phys. Oceanogr., 4, 310-320.

Peffley, M. B., 1974: Oregon near-shore bottom topography digitized. CUEA Newsletter, 3, No. 1, 16-17.

Ryther, J. H., 1969: Photosynthesis and fish production in the sea. Science, 166, 72-76.

Sarkisyan, A. S., and V. F. Ivanov, 1971: Joint effect of baroclinicity and bottom relief as an important factor in the dynamics of sea currents. Izv., Atmospheric and Oceanic Physics, 7, 173-188. (English trans., 116-124).

Scientific Committee on Oceanic Research, 1974: Report of the Second Meeting of SCOR Working Group 36 on Coastal Upwelling Processes. Institut für Meereskunde, Universität Kiel, Federal Republic of Germany, June 24-28, 1974.

Shaffer, G., 1974: On the North West African coastal upwelling system. Ph.D. Thesis, Institut für Meereskunde, Universität Kiel, Federal Republic of Germany, 177pp.

Smith, R. L., 1968: Upwelling. Oceanogr. Mar. Biol. Ann. Rev., 6, 11-47.

Smith, R. L., 1974: A description of current, wind, and sea level variations during coastal upwelling off the Oregon coast, July-August 1972. J. Geophys. Res., 79, 435-443.

Smith, R. L., C. N. K. Mooers, and D. B. Enfield, 1971: Mesoscale studies of the physical oceanography in two coastal upwelling regions: Oregon and Peru. In Fertility of the Sea, 2, edited by J. D. Costlow, Jr., Gordon and Breach, New York.

Stevenson, M. R., R. W. Garvine, and B. Wyatt, 1974: Lagrangian measurements in a coastal upwelling zone off Oregon. J. Phys. Oceanogr., 4, 321-336.

Suginohara, N., 1974: Onset of coastal upwelling in a two-layer ocean by wind stress with longshore variation. J. Oceanogr. Soc. Japan, 30, 23-33.

Thompson, J. D., 1974: The coastal upwelling cycle on a beta plane: hydrodynamics and thermodynamics. Ph.D. Thesis, Florida State University, 141 pp.

Thompson, J. D., and J. J. O'Brien, 1973: Time-dependent coastal upwelling. J. Phys. Oceanogr., 3, 33-46.

Thompson, J. D., and J. J. O'Brien, 1973: Time-dependent coastal upwelling. J. Phys. Oceanogr., 3, 33-46.

Yoshida, K., 1967: Circulation in the eastern tropical oceans with special references to upwelling and undercurrents. Japan. J. Geophys., 4, 1-75.

VITA

Monty Burdette Peffley was born August 12, 1947 in Goshen, Indiana. In 1969 he graduated with distinction from Purdue University at West Lafayette, Indiana with a B.S. in Physics. After serving three years in the U.S. Army, he began his graduate study in the Department of Oceanography at the Florida State University in September, 1972.